Università degli Studi di Roma "La Sapienza"

Facoltà di Ingegneria

Tesi di Dottorato in Elettromagnetismo

Beam Dynamics and Collective Effects in the SPARC Project

Candidato:

Valeria Fusco

Relatore:

Prof. Luigi Palumbo

Correlatori:

Dott. Massimo Ferrario

Dott. Mauro Migliorati

Contents

List of Figures

5

Chapter 1

Introduction

Free electron lasers (FELs) are linac based sources of coherent synchrotron radiation. This chapter briefly describes FELs features.

A FEL is made up of two main system: the undulator, an array of dipoles, which produces synchrotron radiation and the photo-injector that is the electron source.

The Sparc project is a self-amplified-spontaneous emission FEL, that is the synchrotron radiation is induced by the current modulation of the electron beam itself rather than by an external field.

The FEL characteristics strongly depend on the beam quality, achieved in the photo-injector. A high quality beam characterize the 4th generation of synchrotron radiation source; in this case the quality of a beam is described by its emittance, ϵ_n, and its current or in a more compact way by its brightness $B_\perp$. This chapter describes the physical origin (liouville's theorem) and meaning of these important parameters.

As mentioned the high quality beam is achieved in the photo-injector; the main causes of emittance and brightness degradation along the photo-injector and how to compensate them are described here.

Finally the main features of this work are presented in the last section: emittance degradation causes, such as transverse space charge and transverse wake fields, are deeply studied. Such effects have been included in the code

Homdyn which is a very fast semi-analytical code. This tool has been used to improve the beam characteristic of the SPARC project.

1.1 Free-Electron Lasers

1.1.1 Physics of Free Electron Lasers

Synchrotron radiation, the photons produced by charged particles moving in a curved trajectory, is playing an increasingly important role in many areas of basic and applied science.

Synchrotron radiation [1] was first discovered in storage rings: the electrons, after being generated in an electron gun, are bunched, pre-accelerated and then transported into the storage rings. In a storage ring, magnets bend the trajectory of the electrons thus producing synchrotron radiation. An array of strong bending magnets, with alternating field direction, called wigglers, can be used. The radiation produced in all wiggler dipoles adds up incoherently but still provides a much larger amount of radiation than in a single bending magnets. By reducing the magnetic field amplitude, and, as a consequence, the curvature radius of the electron trajectories, the intensity of the radiation can be further increased: the device is called undulator.

Free Electron Lasers (FELs), driven by linacs, constitute the fourth generation of synchrotron light source.

Fig. 1.1 describes the evolution of the radiation in terms of brilliance that is the number of photons per second, frequency interval, area and divergences, versus years.

The first FEL, [2] was built in the middle of 1970 by John Madey and colleagues. Nowadays it is considered a unique tool for scientific applications providing tunable coherent radiation in the far infrared or VUV ranges. Significant effort of scientists and engineers are directed towards the construction of an X-ray laser.
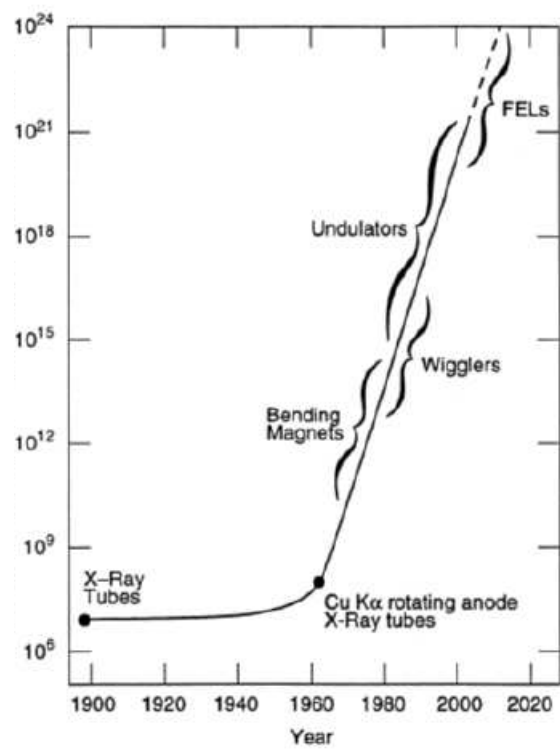
Figure 1.1: *Development of X-ray source brilliance since 1895.*

11
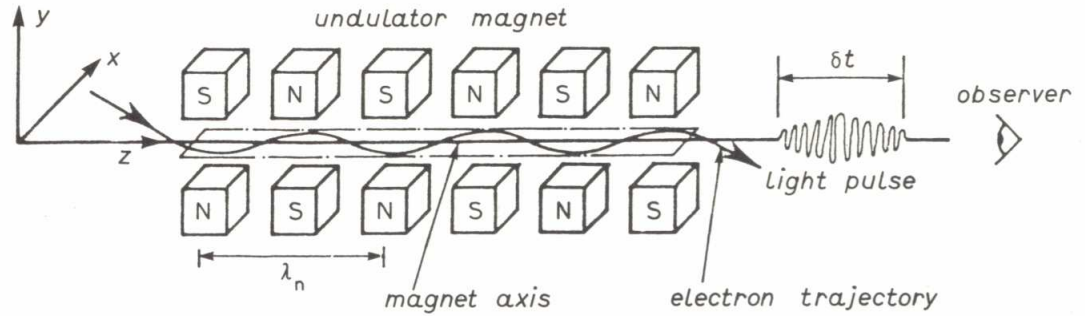
Figure 1.2: *Magnetic undulator in which magnets are arranged to provide a magnetic field that periodically reverses direction.*

As in a storage ring for synchrotron radiation production, a FEL requires an electron beam to be injected into an undulator as in fig. 1.2.

The magnets in the undulator are arranged to provide a magnetic field that periodically reverses direction; the electrons experience the Lorentz force, produced by the magnetic field, and oscillate. At the same time an external field, eventually produced by a laser source, propagates in the same direction as the beam.

The electron beam interacts with the external electric field; some electrons see the external force generated by the electric field opposed to the motion of the electrons: the electrons lose energy which is gained by the external electric field, see fig. 1.3a). On the contrary electrons shifted in phase with respect to the electrons described above, see a force in the same direction as its motion: the electron therefore gains energy from the external field, see fig. 1.3b).

This energy exchange results in the modulation of the longitudinal velocity of the electrons. Therefore electrons that gain energy speed up whilst electrons that lose energy slow down, producing a bunching at the resonant wavelength λ scale
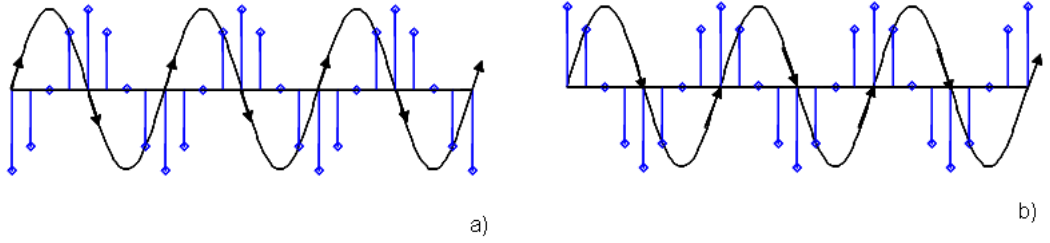
Figure 1.3: *Energy exchange between the electrons (curved line) and the electric field (straight lines). (a) represents electrons loosing energy, (b) the electrons gaining energy.*

$$\lambda = \frac{\lambda_u}{2\gamma}(1 + K^2) \qquad (1.1)$$

where λ_u is the undulator wavelength, γ the electrons energy and $K = eB_u\lambda_u/2\pi mc$ the undulator strength, being B_u the on axis magnetic field, c the speed of light, e and m the electron charge and rest mass respectively.

Finally electrons bunched within a wavelength emit radiation in phase thus producing a coherent intensity. The coherent intensity leads to more energy modulation and more bunching, leading to exponential growth of the radiation. The process ends when the energy lost drives the beam out of resonance.

The production of a coherent radiation in the short wavelength is limited by the external field wavelength. The problem is avoided not using any seeding, that is any external field, to generate the coherent radiation. Self-Amplifying Spontaneous Emission (SASE) FEL uses fluctuations of the electron beam current density as input signal; therefore the radiation can be extended to the X-ray regime.

The main advantage of a FEL over quantum laser is the tunability of the radiation. In the quantum laser, the lasing wavelength is defined by discrete energy transitions between the quantum levels of atoms or molecules of an active medium. As concern the FEL their operating frequency is defined by
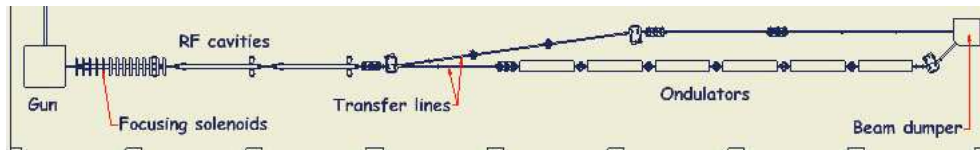
Figure 1.4: *Schematic layout of the SPARC photo-injector including the undulator and by pass line.*

their design, as eq. 1.1 emphasizes, that is by the electron beam energy, the characteristic of the magnetic fields in the interaction region. For these reasons, the FEL can be tuned, in principle,to any desired operating frequency.

Good performances of a FEL depends on the characteristics of the beam at the entrance of the undulator. To achieve short radiation wavelength λ_r and short gain length L_g, which determines the increase of the radiation power along the undulator, we need a high brightness beam, $B_\perp$ (see sec. 1.3), since:

$$\lambda_r \propto \frac{\Delta\gamma}{\gamma}\sqrt{\frac{1+k^2/2}{\gamma B_\perp K^2}} \tag{1.2}$$

$$L_g \propto \frac{\gamma^{3/2}}{K\sqrt{B_\perp(1+K^2/2)}} \tag{1.3}$$

1.1.2 The Sparc Photo-injector

The SPARC (Sorgente Pulsata e Amplificata di Radiazione Coerente) project, [3] is the result of a collaboration of different Italian research institutes, such as INFN, ENEA, CNR.

The Italian Government launched in 2001 a long term initiative devoted to the realization in Italy of a coherent X-ray source, driven by the large interest the 4th generation light sources, as X-ray SASE FELs, have raised world wide in the synchrotron light scientific community, as well as in the particle accelerator community.

14

The SASE FEL experiment, in the Sparc project, is conducted using a permanent magnet undulator made of 6 sections, each 2.1 5m long; the radiation produced will be 500 nm and the power reached after 12 m will be around 10^8 W.

The device preceding the undulator section, called photo-injector, is devoted to the production of a high quality electron beam that is with a low emittance and high current beam (see sec. 1.3).

A photo-injector consists of an electron source and accelerator sections.

The electrons source for Sparc consists of a 1.6 cell RF gun operating in the S-band (2.856 GHz) with a high peak field (120 MV/m). The RF gun includes a metallic photo-cathode which is illuminated by a temporally flat, pico-second laser source. Therefore the laser system driving the photo-cathode employs high bandwidth Ti:Sa technologies with the oscillator pulse train locked to the RF.

The system generates a 5.6 MeV electron beam whose time duration and radius is 10 ps and 1.13 mm respectively. The bunch is then focused by a solenoid whose field peak strength is 0.27 T.

The accelerator device, following the solenoid, is made up of three accelerating traveling wave sections, 3 m long, generating a peak electric field of 25 MV/m, 12.5 MV/m and 12.5 MV/m respectively. The first section is embedded in thirteen solenoid coils, which guarantee the focusing of the beam.

In order to meet the FEL requirements, at the exit of the linac, we obtain a high energy beam, 155 MeV, whose normalized emittance is $\epsilon_n < 2\mu m$, the relative energy spread is $\Delta\gamma/\gamma < 0.1\%$ and the peak current is $I \sim 100A$.

It's worth noting the Sparc project includes also a second beam line, parallel to the one described and represented in fig. 1.4, for bunch compression via magnetic fields. Such study will be very important for the generation of a ultra high brightness, high peak current beam suitable for future X-ray sources.

Bunch charge	1.1nC
Bunch radius	1.13mm
Bunch lenght	10ps
Bunch energy @ gun exit	5.6MeV
Bunch energy @ linac exit	155MeV
Repetition rate	1-10Hz
Cathode peak field	120MV/m
Peak solenoid field @ 0.19m	0,273T

Table 1.1: Relevant parameters in Sparc project.

The scientific case shows a large interest, [4] in the community of synchrotron light users. X-rays from synchrotron light sources are today widely used in atomic physics, plasma and warm dense matter, femtosecond chemistry, life science, single biological molecules, imaging, holography, micro and nano lithography. The high peak brilliance expected with the SASE FEL sources will open new frontiers of research. New techniques in X-imaging can be applied in the field of material science, biology, non linear optics. Of particular relevance are the diffractive techniques with coherent radiation on biologic tissues that allow the single-pulse crystallography of macro molecules.

As already mentioned the performances of a SASE FEL are critically dependent on the quality of the electron beam, thus the main purpose of the Sparc photo-injector is the production of a low emittance high current beam that is a high brightness electron beam before the undulator structure.

1.2 Liouville's Theorem

A beam is made up of a great number of particles so global beam properties are studied instead of analyzing each particle evolution.

Let's consider N particles. In the six-dimension phase space, q_i the canonical space and p_i the momentum coordinates, each particle is represented by a point whilst a beam of particles occupies a volume. The number of particles dN in an elementary volume dV of phase space is given by

$$dN = n(q_1, q_2, q_3, p_1, p_2, p_3)dV \qquad (1.4)$$

where $n(q_1, q_2, q_3, p_1, p_2, p_3)$ is the particle density in the phase space.

The motion of the beam is associated with an equivalent motion of the representative points in the phase space, thus the occupied volume in the phase space changes its shape.

Introducing a velocity vector $\boldsymbol{v} = \{\dot{q}_i, \dot{p}_i\}$ in phase space for each particle and the Hamiltoninan of the system we can obtain, [5]

$$\frac{dn}{dt} = 0 \qquad (1.5)$$

Eq. 1.5 is called Liouville's theorem and it states that, if the number of particles is constant, the density of points in phase space remains constant as well.

It's worth noting the Liouville's theorem is valid when the particles don't interact with each other. In our purpose the interaction of neighbor particles is negligible compared to the average collective fields produced by further (Debey length) particles in the beam.

It's easy to demonstrate the Liouville's theorem also states the volume in the phase space occupied by given particles remains invariant

$$\int\int d^3q_i d^3p_i = const \qquad (1.6)$$

This is also true in the trace space, $x - x'$, $y - y'$, $z - z'$, being x', y', z' the divergence of the beam; besides if there isn't any coupling between the x motion and the other direction the area in the trace space remains constant

$$A_x = \int\int dx dx' \qquad (1.7)$$
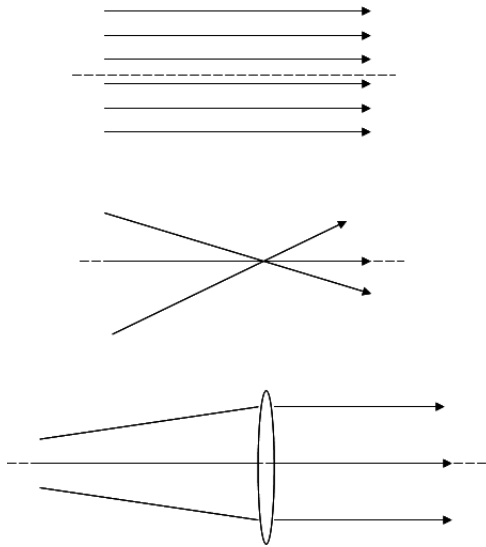
Figure 1.5: *Particle orbits in a laminar beam: ideal parallel beam, converging laminar beam and diverging laminar beam converted to a parallel beam by linear lens.*

This important property led to the introduction of the emittance of a beam.

1.3 Brightness and Emittance

The emittance, [6], [5], [7], is a measure of the quality of a beam. Beam with good parallelism and order are easier to transport and to focus. The ideal charged particle beam has laminar particle orbits, that is orbits in a laminar beam flow in layers that never intersect.

A laminar beam satisfies two conditions: first, all particles at the same transverse position have identical transverse velocities; second, the magnitude of the transverse velocity is linearly proportional to the displacement from the axis of the beam symmetry. If these conditions are not satisfied, the orbits of two particles cross.

Fig. 1.5 shows some examples of particles' trajectory in a laminar beam whilst fig. 1.6 describes some particles' orbit in a non laminar beam.
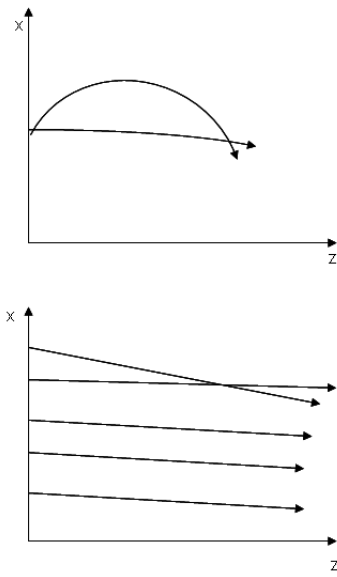
Figure 1.6: 3

Crossing orbits for particles at the same position showing a velocity spread (upper graphics) and for particles whose transverse velocity is not linearly proportional to the displacement from the axis.

The three particles distributions, ideal parallel beam, converging and diverging beam, of fig. 1.5 are depicted in the transverse trace space in fig. 1.7. It's worth noting that for the two conditions mentioned above, the trace space representation of a laminar beam is always a zero thickness straight line.

On the contrary particles in a non laminar beam have a random distribution of transverse velocities at a transverse position: this means a trace space representation wouldn't be a zero thickness straight line but a filled area as in fig. 1.8.

Thus a measure of the parallelism of a beam should be proportional to the area of eq. 1.7.

Such filled area in the $x - x'$, $y - y'$, $z - z'$ trace space, for Liouville's theorem, remains constant if the number of particles remains constant and the coordinates are uncoupled.

Nonetheless, non linear fields, fringing fields and so on in accelerators can modify the shape of the volume stretching and distorting the distribution. Fig. 1.9 represents the progressive distortion of the trace space ellipse during beam propagation when non linear forces acts. The enclosed area remains constant whilst the beam quality get worst.

For this reason the above definition doesn't distinguish between a well-behaved beam, for example in a linear focusing system, and a beam with the same trace space area but a distorted shape due to nonlinear forces.

A definition of the emittance that measure the beam quality rather than the trace-space area is preferred; thus the emittance is defined as a statistical mean area as in [8]

$$\epsilon_x = \sqrt{\left(<x^2><x'^2> - <xx'>^2 \right)} \tag{1.8}$$

A particle distribution along a curved line in the trace space as in fig. 1.10, gives a null area but an emittance which is different from zero.

It's worth noting if there's an energy change, that is $\beta\gamma \neq const$, the
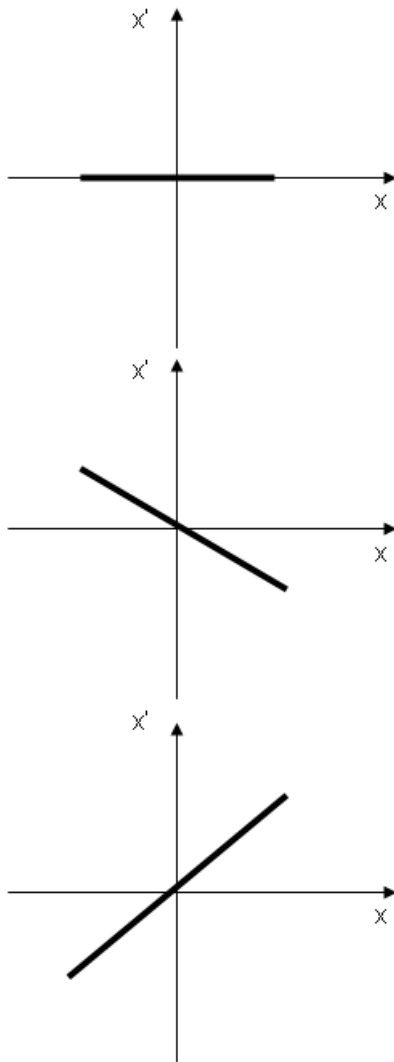
Figure 1.7: *Laminar beam representation in the transverse trace space, for a parallel beam, converging and diverging.*
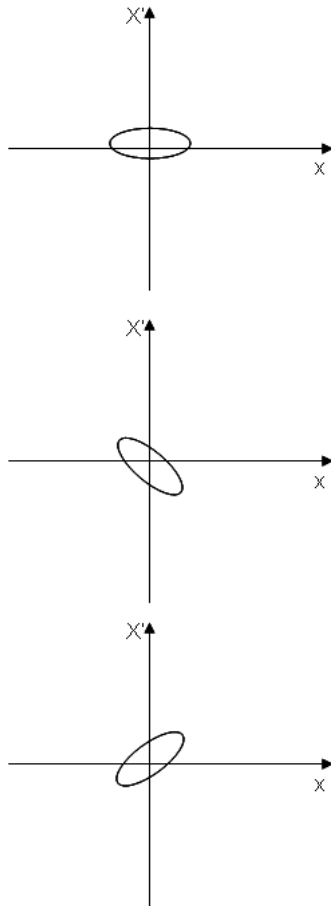
Figure 1.8: *Trace space view of a non laminar beam.*
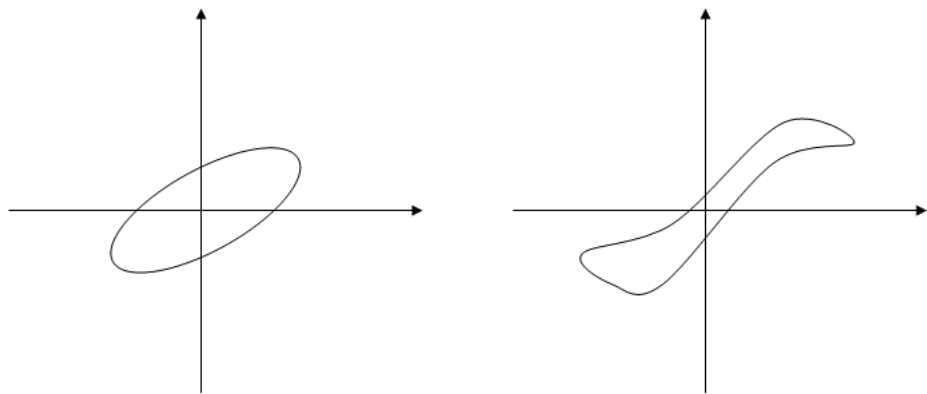
Figure 1.9: *Distortion of the trace space ellipse during beam propagation when non linear forces acts.*

22
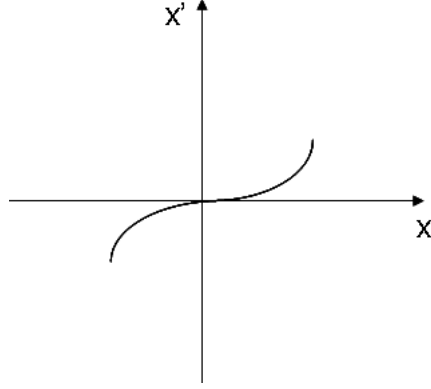
Figure 1.10: *Particles distribution in the trace space along a curved line.*

emittance ϵ_x does not remain constant. For this reason, one introduces the normalized rms emittance

$$\epsilon_{nx} = \beta\gamma\epsilon_x \qquad (1.9)$$

An increase of the normalized emittance is usually an indication that non linear effects, causing a deterioration of beam quality, are present.

As a conclusion, a more complete definition of the normalized emittance includes the case the area is not centered in the origin of the $x - x'$ trace space

$$\epsilon_{nx} = \big(< (x- < x >)^2 >< (\beta\gamma x'- < \beta\gamma x' >)^2 > +$$
$$- < (x- < x >)(\beta\gamma x'- < \beta\gamma x' >) >^2 \big)^{\frac{1}{2}} \quad (1.10)$$

The emittance is an incomplete parameter describing the quality of a beam; infact if we use an aperture to filter out the worst part of a beam, we can focus it to a smaller area but only at expense of the total current I. The current I of a beam is then an important parameter introduced in the so-called transverse brightness of the beam [9]

$$B_\perp = \frac{d^4 I}{dx dx' dy dy'} \qquad (1.11)$$

23

In eq. 1.11 we restricted our attention to the transverse properties of the beam.

The normalized transverse brightness includes in its definition the normalized emittance thus for a uniform beam distribution,we obtain

$$B_{n\perp} = \frac{2I}{\epsilon_{nx}\epsilon_{ny}} \tag{1.12}$$

The meaning of brightness can also be understood by expressing the peak current by the transverse current density $I = J\sigma^2$ and the emittance at a waist as $\epsilon_n = \gamma\sigma\sigma'$, being σ and σ' the rms radius and the rms divergence of the beam respectively. Taking $\epsilon_{nx} = \epsilon_{ny}$ we obtain:

$$B_{n\perp} = \frac{2J}{(\gamma\sigma')^2} \tag{1.13}$$

Thus a high transverse brightness represents a beam propagating with low divergence and high current density.

1.3.1 Emittance degradation

The propagation of a beam trough the device of a photo-injector induces emittance growth. We can distinguish two different causes of emittance degradation: respectively due to transverse non linear fields acting on the bunch and due to longitudinal correlation along the bunch, induced by electromagnetic fields.

The former includes space charge non linearities, as well as RF fields non linearities. As mentioned in the preceding section non linearities generates distortion of the area filled by the beam in the trace space thus increasing the statistical emittance.

The latter includes transverse space charge fields, wake fields and RF fields. Fig. 1.11 represents the bunch in the trace space, when the longitudinal correlation is induced along the bunch. The bunch has been divided into slices; each one is subject to a different transverse force, due to the RF field,
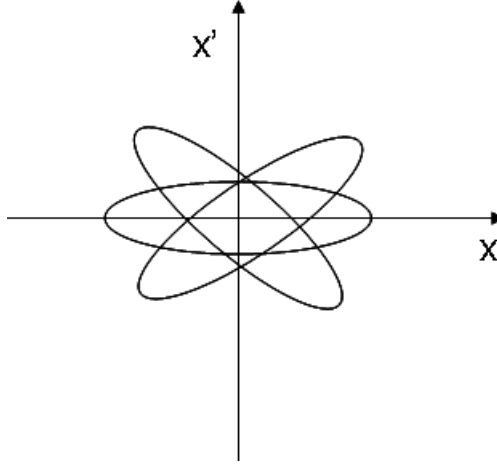
Figure 1.11: *Fan shape of the emittance due to transverse fields induced correlation along the bunch.*

the space charge and the wake fields, so each slice fills a different oriented area in the trace space assuming as a whole a fan shape. The consequence is that even if the emittance of each slice is preserved (if only linear forces are acting), it is not preserved the emittance over the whole bunch.

Emittance growth can be partially compensated as illustrated in the following section. Anyway the theoretical limit of the emittance is represented by the so called thermal emittance; it's the intrinsic emittance existing when the bunch is generated.

Infact conduction electrons in a metal have an energy distribution that obey the Fermi-Dirac statistics. Electrons extracted from the metal cathode belong to the tail of the Fermi-Dirac distribution and have the Maxwell velocity distribution given by

$$f(v_x, v_y, v_z) = f_0 \exp{-\frac{m(v_x^2 + v_y^2 + v_z^2)}{2k_bT}} \tag{1.14}$$

where k_b is Boltzmann constant and T the cathode temperature.

The result is that the particles emerging from the cathode have an intrinsic velocity spread thus an intrinsic emittance. Infact if x and y are the cartesian coordinates perpendicular to the direction of the beam, the rms

velocity spread of the electrons in the bunch emerging from the cathode are

$$< v_x >=< v_y >= \left(\frac{k_b T}{m} \right)^{1/2} \tag{1.15}$$

Moreover if the emitting surface is a circle with radius r_s and with uniform current density, the rms width of the beam is

$$< x >=< y >= \frac{r_s}{2} \tag{1.16}$$

At the waist for a non relativistic beam the normalized emittance is simply given by

$$\epsilon_{nx}^{th} =< x ><\frac{v_x}{c} > \tag{1.17}$$

Substituting eq. 1.15 and eq. 1.16 into eq. 1.17 we obtain the thermal emittance

$$\epsilon_{nx}^{th} = \frac{r_s}{2} \left(\frac{k_b T}{mc^2} \right)^{(1/2)} \tag{1.18}$$

1.3.2 Emittance's Compensation

As previously announced, emittance growth along the photo-injector can be partially compensated.

The laser generating the bunch in the photo-cathode is a temporally flat impulse instead of an easier to generate gaussian impulse, because the bunch's energy is still very low at the exit of the photo-cathode and the bunch undergoes strong space charge forces; transverse space charge forces generated by a uniform bunch affect the emittance less than the space charge forces produced by a guassian bunch; the reason is that the transverse linearity of the space charge fields of a uniform bunch is greater with respect to the gaussian one.

The RF cavity located inside the photo-cathode accelerates the emitted electrons to relativistic energies thus reducing the space charge forces.

Anyway the RF fields themselves give rise to an emittance growth due to the different focusing forces experienced by the slices which have different phase. This emittance degradation is controlled reducing the bunch's dimension which result, anyway, in an increase of the space charge forces.

The correlated emittance growth, due to Both the RF field and the space charge, is compensated by the field of a solenoid placed at the exit of the RF gun: the fan like distribution in the trace space closes itself. It's worth noting the compensation doesn't include the non linearities of the above fields.

To reduce emittance degradation due to space charge, the beam is driven to an accelerating structure which must be properly matched. Infact when the beam is in the space charge regime, mismatches between the space charge forces and the external focusing field produce emittance oscillations. Beams experiences two distinct regimes along the accelerator, depending on the ratio ρ between the space charge force term and the emittance pressure term in the transverse plane (see sec. 4.1)

$$\rho = \frac{I\sigma^2}{2\gamma I_A \epsilon_{th}^2} \tag{1.19}$$

When $\rho \gg 1$ the transverse beam dynamics are dominated by space charge effects and the beam propagated in the quasi-laminar regime in which particle trajectories do not cross each other. By accelerating the beam, a transition occurs to the so-called emittance dominated regime, when $\rho \ll 1$; in this case the transverse beam dynamics are dominated by the emittance and trajectories are not parallel anymore.

It has been shown in [10] when the beam is in the space charge regime the emittance oscillations can be damped when the beam propagates in the subsequent accelerator structure so that the invariant envelope condition

$$\sigma_{INV} = \frac{1}{\gamma'}\sqrt{\frac{2I}{I_A(1 + 4\Omega^2)\gamma}} \tag{1.20}$$

is satisfied, where $\gamma = 1 + T/mc^2$ is the normalized beam kinetic energy
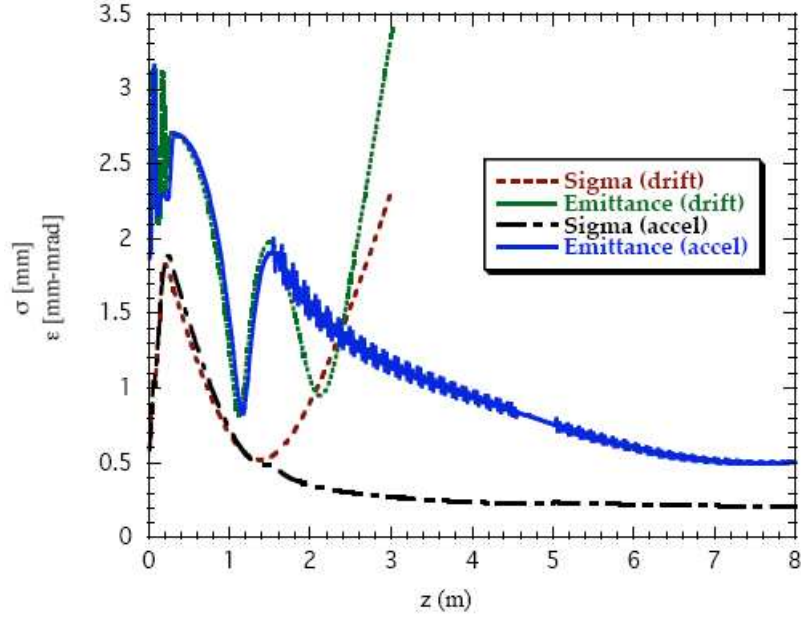
Figure 1.12: *Emittance double minimum behavior, envelope evolution and emittance behavior when accelerating structures are properly matched .*

while the normalized accelerating gradient is defined by $\gamma' \sim 2E_{acc}$, E_{acc} is the accelerating field, I is the beam peak current in the bunch and $I_A = 17kA$ is the Alven current, [5]. Finally the normalized focusing gradient is defined as

$$\Omega^2 = \left(\frac{eB_{sol}}{mc\gamma'}\right) + \begin{cases} \sim 1/8 & \text{Standing Wave} \\ \sim 0 & \text{Traveling Wave} \end{cases}$$

The σ_{INV} is an exact solution of the rms beam envelope equation (see cap.) for a laminar beam, with

$$\sigma'' + \sigma'\frac{\gamma'}{\gamma} + \sigma\frac{\Omega^2\gamma'^2}{\gamma^2} - \frac{I}{2I_A\sigma\gamma^3} = \frac{\epsilon^{th2}}{\sigma^3\gamma^2} \sim 0 \qquad (1.21)$$

Following such theory, that is injecting the beam at a laminar waist, a new working point was found in [11]. By increasing the solenoid magnetic field, the emittance shows a double minimum behavior along the horizontal axis as in fig. 1.12

If the accelerating structure is placed where the emittance exhibits its maximum then the second emittance minimum can be frozen and translated at the exit of the accelerating section.

It is interesting to note that the double minimum in the emittance is due to a chromatic effect inside the solenoid device [11]. Infact each slice has a different energy γ and the different position along the bunch experience a different focusing solenoidal field. As a consequence only one slice has the right γ to satisfy the invariant envelope condition whilst all the other slices oscillate around the equilibrium envelope equation. The different oscillation of the slices generates a beating term which give rise to the emittance double minimum as explained in [12].

Finally transverse wake fields in the accelerating structures generates correlated emittance degradation as explained in the previous section. A technique, called beam based alignment, compensates emittance degradation caused by wake fields; it consists in the use of steering magnets to realign the bunch on the axis of each structure thus canceling the transverse wake fields.

1.4   Purpose of the study

Space charge and wake fields are also called collective effects: both are the result of the Coulomb forces in a multi-particle system.The space charge is the electromagnetic field produced by a bunch moving in free space; the wake field is the electromagnetic field produced in an enclosed space, with a non uniform shape and/or a finite resistive wall, by a charge traveling with speed of light. They are called wake fields because they can neither act on the charge itself nor on any charges in front of it but only on charges lying behind it.

The aim of this work is the study of such phenomena in the Sparc project, the improvement of the Homdyn code including off axis beam dynamics and

finally the study of emittance degradation. The code Homdyn [11] is a semi-analytical code which is very fast with respect well-known multi-particles code such as Parmela. Such code has been improved including off axis beam dynamics in which space charge on the centroid of the bunch and transverse wake fields are considered.

The improved version of the Homdyn code, [13], [14]allow to study emittance degradation due to misalignments along the photo-injector, to develop a correction scheme for the SPARC project to control the bunch's trajectory and angle and to study the emittance and energy spread degradation in the emittance measurements experiment.

Cap. 2 describes the electric field produced by a bunch moving in free space for different bunch's charge distribution. In particular we analyze the case of a cylindrical finite length bunch with circular and elliptical section. Significant effort is given to the elliptical section case, [15], infact the focusing properties of some accelerator devices, as quadrupoles and bending magnets, can change the charge distribution of a bunch from round to elliptical. A general rule allows to associate the electric field on the axis of a round infinite bunch to the electric field of an infinite elliptical one: the numerical solution demonstrates this is not always true for a finite bunch length. Anyway the Sparc project's first phase deal with a bunch whose eccentricity remains low enough: thus the general rule can still be used.

Cap. 3 briefly summarize the general definition of the longitudinal and transverse wake fields, [16]. The geometric dimensions of the linac cavities and the short bunch length involved in the Sparc project allow the use of the diffraction model, [17], for the analytical solution of the wake fields in a single cavity. The case of a periodic collection of cavities is also solved.

Cap. 4 describes the beam dynamics in the Homdyn code and the improvements achieved. The main approximation in the code lies in the assumption the bunch is a uniformly charged cylinder; the cylinder is divided in slices and the code follows the evolution of each slice, using the envelope

equation. When the bunch is generated off-axis, transverse time dependent fields can misalign neighbor slices. Thus an equation of motion for each slice' centroid motion, transverse and longitudinal, is also inserted in the Homdyn code. In this case wake fields and space charge are included. A bunch traveling in a solenoid field is also considered. The envelope equation and the emittance computation is described.

In cap. 5 the Homdyn code is finally used to study the misalignments in the Sparc project. First of all the off axis beam dynamics is applied to the study of the emittance meter experiment, [18]. The movable emittance meter experiment's aim is to measure the emittance just outside the gun along the z axis. A bellow moves the emittance meter; such bellow, made up of triangular cavities, generates longitudinal wake fields and transverse wake fields when the bunch is misaligned with respect the bellow axis. Emittance degradation is then studied. Finally we analyze a correction scheme using steering magnets to correct the centroid orbit and minimize the emittance, [13]. Different techniques are used, among these the beam based alignment technique [19].

Chapter 2

Space Charge

The net effect of the Coulomb interactions in a multi-particle system can be classified into two regimes: collisional regime and space charge regime. The former is dominated by binary collisions caused by close particle encounters: these are called single particle effects. The latter is dominated by self fields produced by the particle distribution, which varies appreciably only over large distances compare to the average separation of the particles: these are called collective effects.

A measure for the relative importance of collisional versus collective effects is the Debye length λ_D which represents the effective interaction range: smooth functions for the charge and field distributions can be used as long as the Debye length remains small compared to the particle bunch size.

We study in this chapter the collective effect known as space charge, that is the electric field produced by a bunch moving in free space; we will consider the case of a bunch moving in enclosed space in Cap. 3.

We study different bunch's charge distribution; effort is given to the case of a cylindrical space charge distribution whose section is elliptical. Infact the focusing properties of different accelerators devices, as quadrupoles and bending magnets, can change the charge distribution of a bunch from round to elliptical one. Depending on the intensity of this effect, the dynamics properties of the bunch could be affected. The consequent increase of the

design emittance, reduces the performances of the machine.

We describe how to obtain the electric field of a uniformly charged infinite cylinder, with circular and elliptical cross section.

We derive the on axis longitudinal and radial electric field of a uniformly charged cylinder with circular cross section and finite length. The cylinder is moving along the z axis at velocity v. For the longitudinal electric field an exact solution can be obtained, whilst for the radial electric field only an approximate solution is derived limited to a radial linear dependence.

Then we obtain an integral expression of the on axis longitudinal and radial electric field of a bunch moving along the $z$axis at velocity v and shaped like a uniformly charged finite cylinder having an elliptical cross section. Furthermore we derive an approximate solution of the longitudinal electric field by a series expansion of the integral expression.

Finally we solve numerically the above equations and compare the numeric solutions of the integrals with approximate formulas. Moreover it is well known that for an infinite bunch with elliptical cross section, the radial electric field calculated on the two semi axis a and b, is equal to the radial electric field of an infinite bunch with circular cross section of radius $r = (a + b)/2$.We show that this general rule cannot be applied for finite distributions.

We relate the electric fields behavior of a finite length bunch with the so called aspect ratio defined as $A = R/\gamma L$, where R is the bunch radius, L its length and γ the relativistic parameter.

2.1 Infinite Cylinder with Circular and Elliptical distribution

The electric field of a circular cross section charged cylinder with infinite length can be easily derived form Gauss's law:

$$\int_S \epsilon_0 \boldsymbol{E} \cdot d\boldsymbol{S} = \int_V \rho dV \tag{2.1}$$

which gives inside the cylinder

$$E_r = \frac{\rho}{2\epsilon_0} r \tag{2.2}$$

being ρ the bunch's charge density in the laboratory frame. The electric field of an elliptical cross section cylinder with infinite length can be derived following [11]. Starting from the potential of an ellipsoid of semi axis a, b, c and charge density ρ with $c \to \infty$, we obtain the potential of an infinite cylinder with elliptical cross section moving at velocity v. From the potential we get the radial electric field inside the cylinder [20],[6], [21], [22], [7], [23].

$$E_x = \frac{\rho}{\epsilon_0} \frac{bx}{a+b} \tag{2.3}$$

$$E_y = \frac{\rho}{\epsilon_0} \frac{ay}{a+b} \tag{2.4}$$

Only the radial electric field exists since the longitudinal electric field is zero for an infinite distribution. It is important to note that the electric fields component on the cylinder axes, in a and b, are the same, that is $E_{x=a} = E_{y=b}$, and they are equal to the electric field generated by an infinite cylinder with circular cross section, eq. 2.2, calculated in $r = (a+b)/2$

In sec. we will demonstrates the same method cannot always be used in the case of a finite distribution.

2.2 Finite Cylinder with Circular Cross Section

The longitudinal and radial electric field for a circular cross section finite cylinder are, [11]:
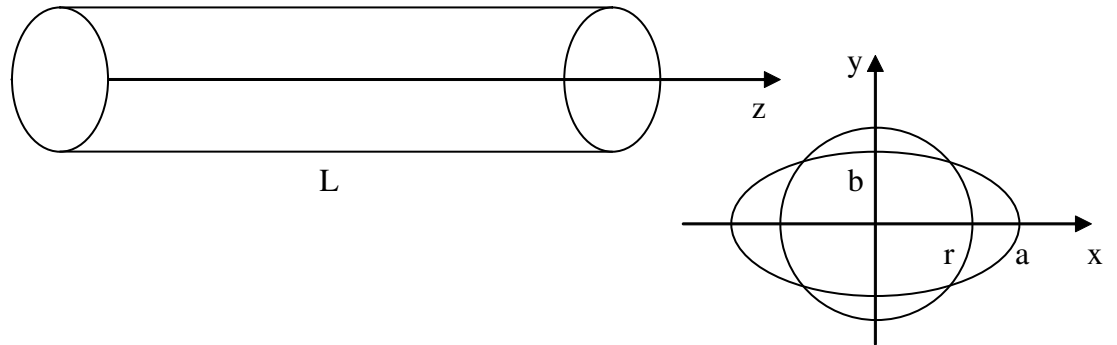
Figure 2.1: *Uniformly charged bunch of finite length L, with elliptical (semi axis a and b) and circular cross section (radius r = (a + b)/2)*

$$E_z(z, r = 0) = \frac{\rho}{2\epsilon_0 \gamma}[\sqrt{R^2 + \gamma^2(L - z)^2} - \sqrt{R^2 + \gamma^2 z^2} + \gamma|z| - \gamma|z - L|] \quad (2.5)$$

and

$$E_r(r, z) = \frac{\rho\gamma}{4\epsilon_0}r[\frac{L - z}{\sqrt{r^2 + \gamma^2(L - z)^2}} + \frac{z}{\sqrt{r^2 + \gamma^2 z^2}}] \quad (2.6)$$

where r is the radial coordinate, L the bunch's length,R and ρ its radius and charge density respectively. The longitudinal electric field is calculated on the bunch's axis z, whilst the radial electric field is obtained from the on axis longitudinal electric field by a linear expansion, considering linear terms in r, [15]. As a consequence eq. 2.6 is an approximation and its accuracy increases with longer bunch.

The longitudinal and radial electric field, generated by the estimated bunch of the SPARC project, is shown in fig. 2.2. The longitudinal electric field grows inside the bunch and its absolute value is at its maximum on the bunchs head and tail, whilst the radial one is at his maximum in the center of the bunch.
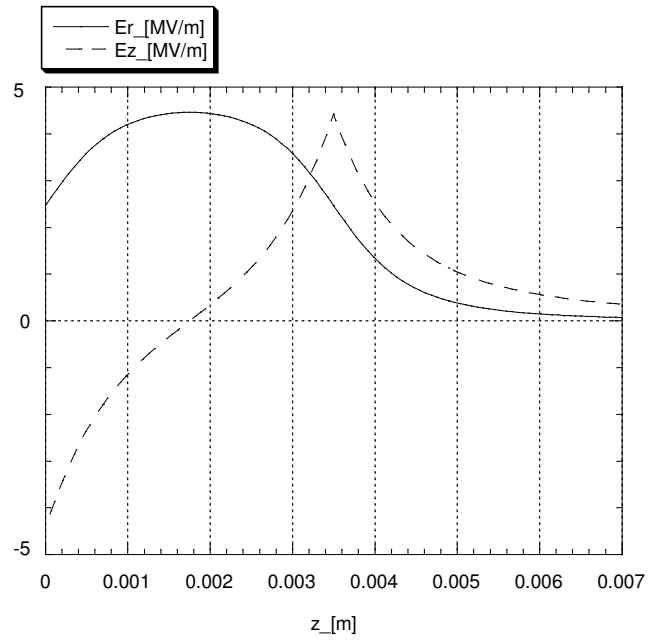
Figure 2.2: *Longitudinal (dashed line) and radial (continuous line) electric field of a bunch of length $L = 3.4mm$, circular cross section of radius $r = 1mm$, charge $Q = 1nC$ and relativistic factor $\gamma = 1$.*

2.3 Finite Cylinder with elliptical cross section

The procedure used to calculate the longitudinal and radial electric field of a bunch with elliptical cross section is similar to that explained in the previous section. To this purpose we can use eq. 2.7 to calculate the longitudinal electric field:

$$E_z(z, r = 0) = \frac{\rho}{4\pi\epsilon_0\gamma} \int_0^{2\pi} \left[\sqrt{R^2 + \gamma^2(L-z)^2} - \sqrt{R^2 + \gamma^2 z^2} + \right.$$

$$\left. + \gamma|z| - \gamma|z - L| \right] d\phi \quad (2.7)$$

The radius r', in the elliptic case, is not constant but depends on the angle ϕ as:

$$r'^2 = \frac{b^2}{1 - e^2 cos^2\phi} \quad (2.8)$$

where the eccentricity of the ellipse is $e = \sqrt{1 - b^2/a^2}$ the eccentricity of the ellipse is $e = \sqrt{1 - b^2/a^2}$. It can be easily verified that as L approaches infinite the longitudinal electric field goes to zero. To simplify the integral eq. 2.7 we expand eq. 2.8 in e, up to the fourth order:

$$r'^2 = \frac{b^2}{1 - e^2 cos^2\phi} \approx b^2(1 + e^2 cos^2\phi + e^4 cos^4\phi + ...) \quad (2.9)$$

The second order approximation can be easily derived; that is we neglect the fourth order term in the expansion eq. 2.9 and solve the corresponding integral of eq. 2.7 obtaining

$$E_z = \frac{\rho}{\pi\epsilon_0\gamma} \left\{ \alpha E[\Gamma^2] - \beta E[\Lambda^2] - \frac{\rho}{2\epsilon_0}[|L - z| - |z|] \right\} \quad (2.10)$$

with

$$\alpha = \sqrt{b^2(1+e^2) + \gamma^2(L-z)^2} \qquad (2.11)$$

$$\beta = \sqrt{b^2(1+e^2) + \gamma^2 z^2}$$

$$\Gamma^2 = \frac{b^2 e^2}{b^2(1+e^2) + \gamma^2(L-z)^2}$$

$$\Lambda^2 = \frac{b^2 e^2}{b^2(1+e^2) + \gamma^2 z^2}$$

and

$$E[x^2] = \int_0^{\pi/2} \sqrt{1 - x^2 sin^2\phi}\, d\phi$$

Moreover if we keep the fourth order term in eq. 2.9, the square roots of eq. 2.7 become

$$\sqrt{b^2 + k^2}\sqrt{1 + \frac{b^2}{b^2 + k^2}(e^2 cos^2\phi + e^4 cos^4\phi)} \qquad (2.12)$$

$$\sqrt{b^2 + k'^2}\sqrt{1 + \frac{b^2}{b^2 + k'^2}(e^2 cos^2\phi + e^4 cos^4\phi)} \qquad (2.13)$$

where

$$k^2 = \gamma^2(L-z)^2 \qquad (2.14)$$

$$k'^2 = \gamma^2 z^2$$

We can expand the square root eq. 2.12 as

$$\sqrt{b^2 + k^2}\left[1 + \frac{1}{2}\left(\frac{b^2}{b^2 + k^2}\right)(e^2 cos^2\phi + e^4 cos^4\phi) + .\right]$$
$$- \frac{1}{8}\left(\frac{b^2}{b^2 + k^2}\right)^2 (e^2 cos^2\phi + e^4 cos^4\phi)^2 +$$
$$- .\left[\frac{3}{48}\left(\frac{b^2}{b^2 + k^2}\right)^3 (e^2 cos^2\phi + e^4 cos^4\phi)^3\right] \quad (2.15)$$

Expanding the square and the cube in the above expression and keeping the term up to the fourth order we have:

$$\sqrt{b^2 + k^2}\left[1 + \frac{1}{2}\left(\frac{b^2}{b^2 + k^2}\right)e^2 cos^2\phi + \left(\frac{b^2(3b^2 + 4k^2)}{8(b^2 + k^2)^2}\right)e^4 cos^4\phi\right] \quad (2.16)$$

The same can be done for eq. 2.13 getting eq. 2.16 with k replaced by k'

$$\sqrt{b^2 + k'^2}\left[1 + \frac{1}{2}\left(\frac{b^2}{b^2 + k'^2}\right)e^2 cos^2\phi + \left(\frac{b^2(3b^2 + 4k'^2)}{8(b^2 + k'^2)^2}\right)e^4 cos^4\phi\right] \quad (2.17)$$

Eq. 2.16 and eq. 2.17 can be inserted in the integral eq. 2.7 and solved easily with respect to the variable ϕ thus obtaining the fourth order approximation for the longitudinal electric field

$$E_z(z,0) = \frac{\rho}{4\pi\epsilon_0\gamma}\left\{\sqrt{b^2 + k^2}\left[2\pi + \frac{b^2\pi}{2(b^2 + k^2)}e^2 + \frac{3b^2\pi(3b^2 + 4k^2)}{32(b^2 + k^2)}e^4\right] - \right.$$
$$\left. \sqrt{b^2 + k'^2}\left[2\pi + \frac{b^2\pi}{2(b^2 + k'^2)}e^2 + \frac{3b^2\pi(3b^2 + 4k'^2)}{32(b^2 + k'^2)}e^4\right]\right\} \quad (2.18)$$

The radial electric field on the contrary can't be obtained from the longitudinal one as in the previous case. For an elliptical cross section, in fact, it does not exist any ϕ angle symmetry. For this reason we calculate the radial electric field referring to fig. 2.3:

$$\boldsymbol{E} = \frac{q(1 - \beta^2)}{4\pi\epsilon_0 r^2(1 - \beta^2 sin^2\theta)^{3/2}\hat{r}} \quad (2.19)$$

With some mathematics we get

$$E_r = \iiint \frac{\rho\gamma}{4\pi\epsilon_0}\frac{\bar{S}P'cos\alpha}{\left(\gamma^2(z - l)^2 + \bar{S}P'^2\right)}\sigma d\sigma d\phi dl \quad (2.20)$$

with

$$0 < l < L$$

39
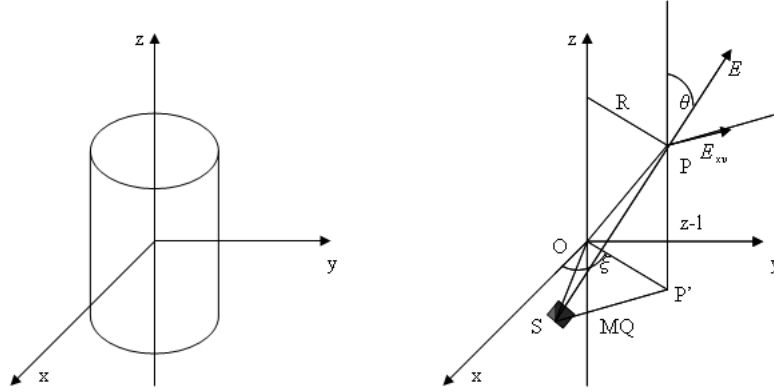
Figure 2.3: *3D-coordinate system used to calculate the radial electric field of a uniformly charged cylinder with elliptical cross section.*

$$0 < \sigma < \sqrt{\frac{b^2}{1 - e^2 cos^2\phi}}$$

$$0 < \phi < 2\pi$$

and

$$\bar{SP'} = \sqrt{\sigma^2 + R^2 - 2\sigma R cos(\xi - \phi)} \tag{2.21}$$

R is the observer's distance from the bunch center and ξ the angle between the observer and the x axis.

Eq. 2.20 can be solved with respect to the coordinate l, thus obtaining:

$$dE_r = \frac{\rho\gamma}{4\pi\epsilon_0} \frac{1}{\bar{SP'}} \left[\frac{z}{\sqrt{\gamma^2 z^2 + \bar{SP'}}} - \frac{z - L}{\sqrt{\gamma^2(z - L)^2 + \bar{SP'}}} \right] \cos\alpha\sigma d\sigma d\phi$$

Using

$$\bar{SP'} = \sqrt{\sigma^2 + R^2 - 2\sigma R \cos(\xi - \sigma)} \tag{2.22}$$

and

40

$$\cos\alpha = \frac{-\sigma^2 + \bar{SP'}^2 + R^2}{2\bar{SP'}R} = \frac{R - \sigma\cos(\xi - \phi)}{\sqrt{R^2 + \sigma^2 - 2R\sigma\cos(\xi - \phi)}}$$

eq. 2.20 becomes:

$$E_r(R, \xi, z) = \frac{\rho\gamma}{4\pi\epsilon_0}[zI_1 - (z - L)I_2] \qquad (2.23)$$

with

$$I_1 = \iint \frac{\sigma(R - \sigma\cos(\xi - \phi))}{(R^2 + \sigma^2 - 2R\sigma\cos(\xi - \phi))\sqrt{\gamma^2 z^2 + R^2 + \sigma^2 - 2R\sigma\cos(\xi - \phi)}}d\sigma d\phi$$

$$I_2 = \iint \frac{\sigma(R - \sigma\cos(\xi - \phi))}{(R^2 + \sigma^2 - 2R\sigma\cos(\xi - \phi))\sqrt{\gamma^2 (z - L)^2 + R^2 + \sigma^2 - 2R\sigma\cos(\xi - \phi)}}d\sigma d\phi$$

and

$$0 < \sigma < \sqrt{\frac{b^2}{1 - e^2\cos\phi}}$$

$$0 < \phi < 2\pi$$

Eq. 2.23 represents the radial electric field an observer sees if he is placed at a distance R from the bunch center with an angle ξ respect to the x axis coordinate and at a distance z from the bunchs tail. It has been verified numerically that as L approaches infinite eq. 2.23 approaches the electric fields of an infinite elliptical cylinder (eq. 2.3 and eq. 2.4)

2.4 Comparison Between Numerical and An-alytical Field

The two approximations of eq. 2.10 and eq. 2.18 for the longitudinal electric field can be compared with the numerical solution of eq. 2.7 and with the
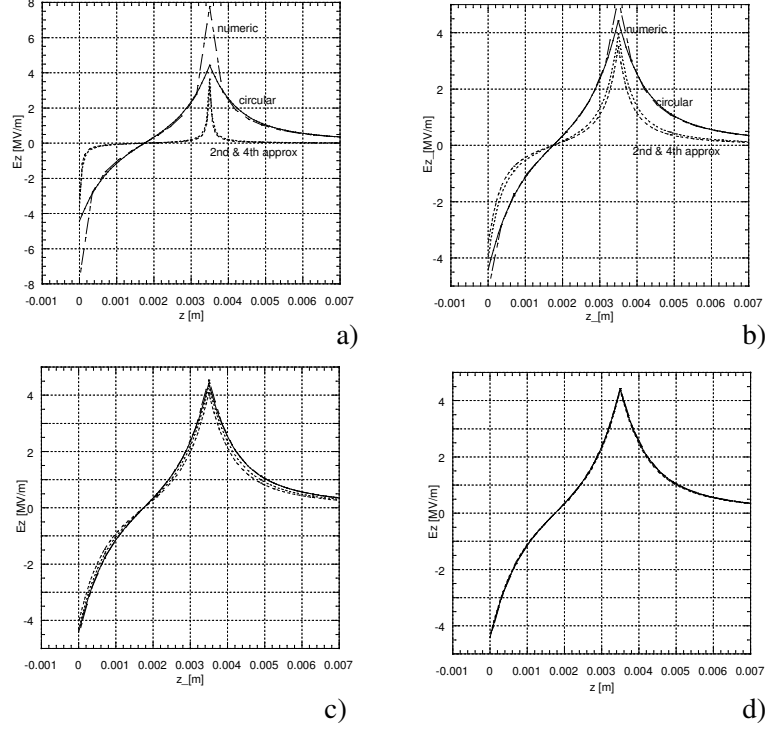
Figure 2.4: *Comparison between the longitudinal electric field obtained numerically (dashed line), the longitudinal electric field of the circular cross section case with $r = (a+b)/2$ (continuous line) and the longitudinal electric field approximated by the 2nd and the 4th order terms (dotted line). The length, the charge and the relativistic factor are the same of fig. 2.2; the eccentricity is (a) $e = 0.999671$ (b/a = 0.026) , (b) $e = 0.979055$ (b/a = 0.2), (c) $e = 0.830901$ (b/a = 0.556) , (d) $e = 0.56296$ (b/a = 0.826).*

longitudinal electric field of the circular cross section cylinder with $r = (a + b)/2$. Fig. 2.4 shows the comparison for different values of the eccentricity:

When the eccentricity is zero, that is the bunch has a circular cross section, all the graphs coincide; more the eccentricity approaches to unity, more the graphs draw away. For all the different eccentricitys values, the circular cross section bunch electric field (continuous line) is the closest to the numerical solution, as can be seen form fig. 2.4. Fig. 2.5 shows a comparison between the radial electric field obtained numerically from the above eq. 2.23, on the semi axis a $(\xi = 0)$ and b $(\xi = \pi/2)$, and eq. 2.6, that is the radial electric field for a circular cross section finite bunch whose radius is $r = (a + b)/2$.

In the case of an elliptical cross section finite bunch, as can be seen from the figures, the radial electric field calculated on the major semi axis, $x = a$, is different from the one calculated on the minor semi axis, $y = b$. The radial electric field in $x = a$ is close to the circular cross section one even for high eccentricity; meanwhile the one calculated in $y = b$ is still far from the approximation for lower eccentricity. Of course as the eccentricity approaches to zero all the plots become closer; when the eccentricity is zero the fields, calculated on the two semi axis, are of course the same. It is important to note that, since the radial electric field of eq. 2.6 is an approximation, the fields of fig. 2.5e do not coincide perfectly.

2.5   Role of the Aspect Ratio Parameter in the Field Form Factor

We can explain the radial fields different behavior on the two semi-axis, with respect to the infinite length case, observing that in this case the length of the bunch plays an important role. When the eccentricity is close to unity then $b << L$ and as a consequence the fields behavior is similar to that of an
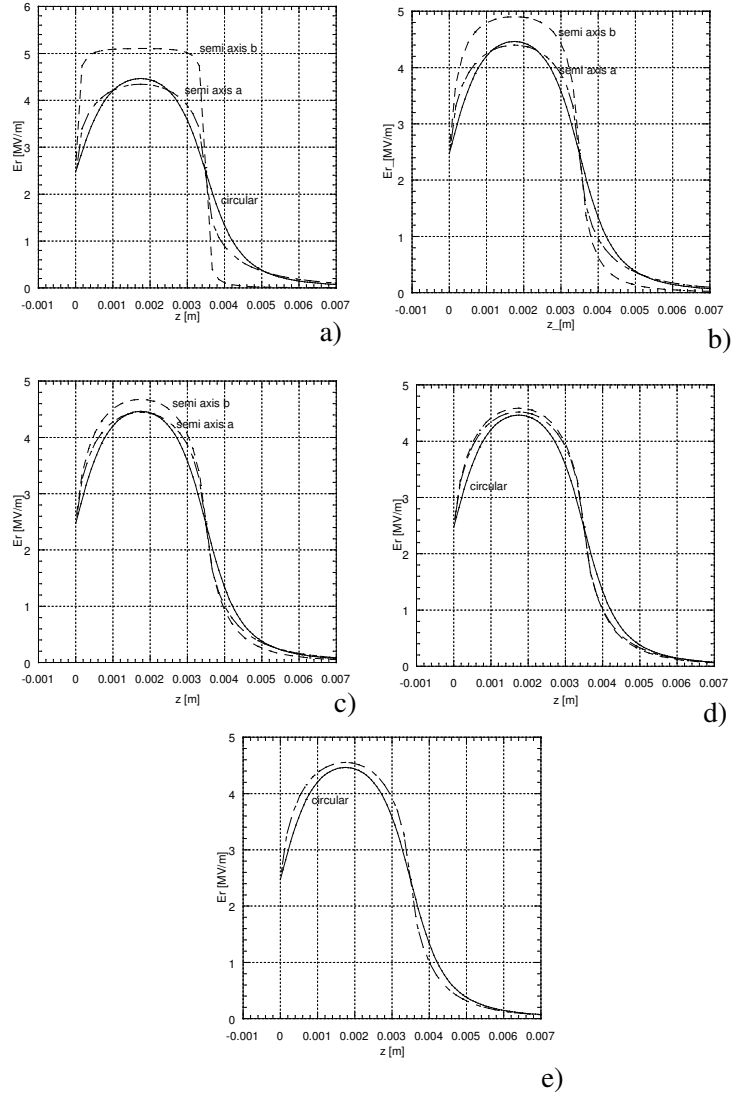
Figure 2.5: *Comparisons between the radial electric field obtained numerically on the semi axis a and b ($\xi = 0$ and $\xi = \pi/2$ respectively) (dashed lines), the radial electric field of the circular cross section case with $r = (a + b)/2$ (continuous line). The length, the charge and the relativistic factor are the same of fig. 2.2; the eccentricity is (a) $e = 0.999671$ (b/a = 0.026), (b) $e = 0.979055$ (b/a = 0.2), (c) $e = 0.830901$(b/a = 0.556), (d) $e = 0.56296$ (b/a = 0.826), (e) $e = 0$ (b/a = 1).*
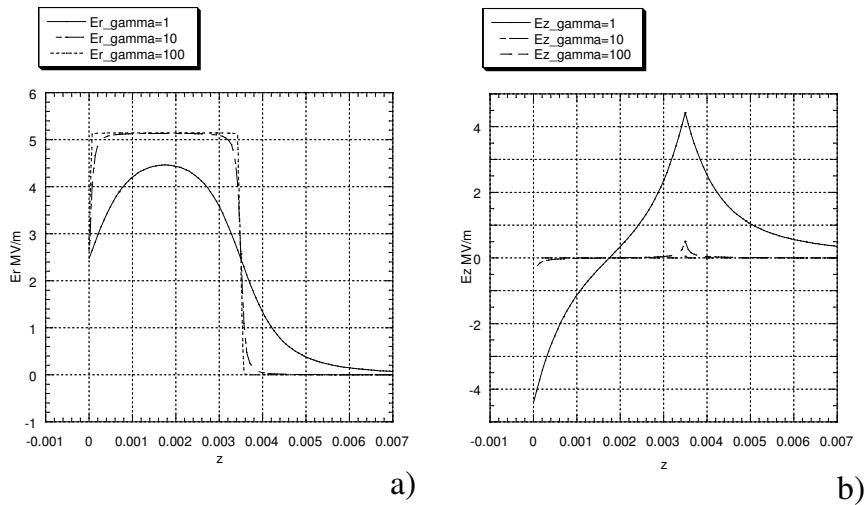
Figure 2.6: *Radial (a) and longitudinal (b) electric field for a circular cross section bunch. The length and the charge of the bunch are the same of fig. 2.2.*

infinite bunch, that is it is constant with the longitudinal coordinate z and shows a discontinuity as it reaches the edges of the bunch. On the contrary since a is comparable to the bunch length L its behavior is different from an infinite bunch. As L approaches zero we obtain the radial electric field of an elliptical disk uniformly charged. Using eq. 2.23 we can numerically verify that the radial electric field in $x = a$ and $y = b$ are still different. Besides the bunch is moving with a velocity v along the z axis, so when its velocity increases, or the relativistic parameter γ increases, the radial electric field becomes more and more squared. Of course the same behavior can be obtained for a circular cross section bunch as well, just increasing its length or increasing its relativistic parameter γ as shown in fig.7. Note that the longitudinal electric field approaches zero as for an infinite bunch.

It follows from the above explanation that the field's behavior in $x = a$ and $y = b$ depends on the size of the ellipse's semi axis with respect to the

45

bunchs length or its relativistic parameter γ, that is on the so called aspect ratio, [24]:

$$A = \frac{R}{\gamma L} \qquad (2.24)$$

where R is the major semi axis a or the minor semi axis b. We deduce that as the aspect ratio decreases the electric field becomes more and more squared.

The longitudinal and radial electric field, for a circular cross section bunch, as a function of the aspect ratio, can be easily obtained. For an elliptical cross section cylinder the fields can be written as a function of the aspect ratio as well:

$$E_r(A, \xi, z) = \frac{\rho \gamma L}{4\pi\epsilon_0}[\frac{z}{L}I_1 - \left(\frac{z}{L} - 1\right) I_2] \qquad (2.25)$$

$$E_z(z, 0) = \frac{\rho L}{4\pi\epsilon_0} \int 0_{2\pi} \left[\sqrt{u^2 + \left(1 - \frac{z}{L}\right)^2} - |1 - \frac{z}{L}|1 - \frac{z}{L}| \right] d\phi \qquad (2.26)$$

where

$$I'_1 = \int\!\!\int \frac{s[A - s\cos(\xi - \phi)]}{[A^2 + s^2 - 2As\cos(\xi - \phi)]\sqrt{\left(\frac{z}{L}\right)^2 + A^2 + s^2 - 2As\cos(\xi - \phi)}} ds d\phi$$

$$I'_2 == \int\!\!\int \frac{s[A - s\cos(\xi - \phi)]}{[A^2 + s^2 - 2As\cos(\xi - \phi)]\sqrt{\left(\frac{z}{L} - 1\right)^2 + A^2 + s^2 - 2As\cos(\xi - \phi)}} ds d\phi$$

and

$$u^2 = \frac{\left(\frac{b}{\gamma L}\right)^2}{1 - e^2\cos^2\phi}$$

$$s = \frac{\sigma}{\gamma L}$$

46

$$0 < s < \sqrt{\frac{\left(\frac{b}{\gamma L}\right)^2}{1 - e^2 \cos^2 \phi}}$$

$$0 < \phi < 2\pi$$

From the previous considerations we deduce that the longitudinal electric field of a finite length bunch with elliptical cross section is well approximated by the longitudinal electric field of a finite length bunch with circular cross section and radius $r = (a + b)/2$. On the contrary the radial electric fields on the envelope $x = a$ and $y = b$ become more and more different as the aspect ratio A increases and the circular approximation cant be used anymore. Fig. 2.7 shows the ratio between the two radial fields when the aspect ratio grows for different eccentricity's value. The aspect ratio in fig. 2.7 is $A = a/(\gamma L)$.

Note that when the eccentricity decreases the ratio between the two fields becomes closer to unity even for a higher aspect ratio.

2.6 Conclusions and Applications to the Sparc project

We reviewed the analytical formulas for the electric field generated by a cylindrical bunch either of infinite length with elliptical cross section and of finite length with circular cross section. Moreover, we obtained the electric field of a finite length bunch with elliptical cross section and compared its numerical solution with the electric field of a circular cross section bunch of finite length whose radius is $r = (a + b)/2$. Even if this rule fits the infinite cylinder case, it is not appropriate for the finite cylinder case, unless the eccentricity is lower than 0.8 for $\gamma = 1$.

The different behavior of these two cases can be explained by the aspect ratio $A = R/\gamma L$. In particular the radial electric field of a finite bunch

47
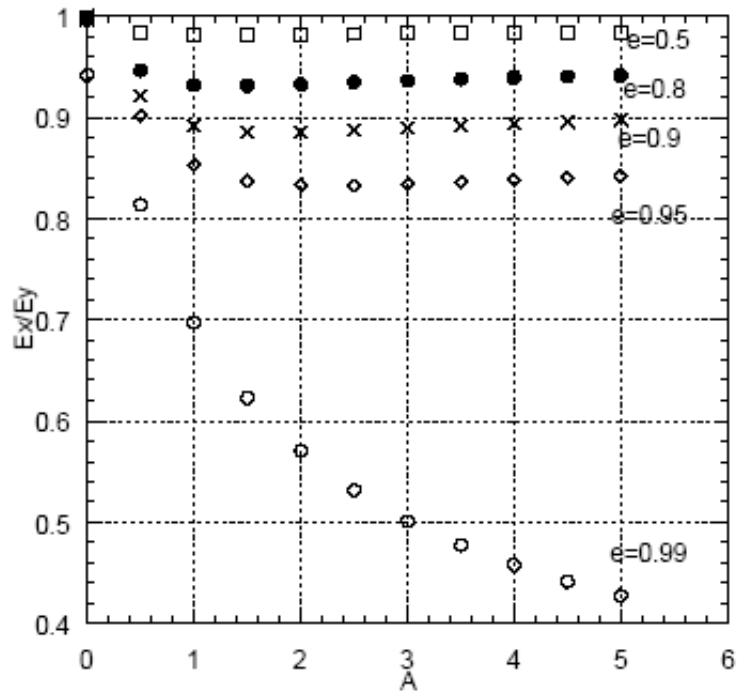
Figure 2.7: *Ratio between the radial electric field in $x = a$ and $y = b$ in $z = L/2$ as a function of the aspect ratio A for different eccentricity $e = 0.999671$ (b/a = 0.026), e = 0.95 (b/a = 0.31), e = 0.9 (b/a = 0.43), e = 0.8 (b/a = 0.6) and e = 0.5 (b/a = 0.866).*

becomes that of an infinite bunch when A becomes small, that is when the length or γ increases. For example, for a very high eccentricity ($e = 0.99$) but small aspect ratio ($A = 0.01$) the circular cross section approximation can still be used.

The Sparc project's first phase deal with small eccentricity bunch and high aspect ratio. This means the general rule that uses the circular cross section transverse electric field can still be applied.

This won't be true in the Sparc project's second phase; in this case a high eccentricity bunch is produced and the general rule can't be applied anymore.

Chapter 3

Wake Fields in the SPARC Photo-injector and Linac

Let's consider a point charge Q (the leading charge) moving in free space ; if the charge Q is moving at a velocity close to the speed of light, a test charge q (the trailing charge) situated in front of or behind the particle, doesn't experience any electromagnetic force because the electric field lines lie in a transverse plane with an opening angle of the order of $1/\gamma$ as in fig. 3.1

The same happens if the leading charge in fig. 3.2 is traveling along a perfectly conducting wall at a velocity close to the speed of light: the image charge, on the conducting wall, will travel at the same velocity of the leading
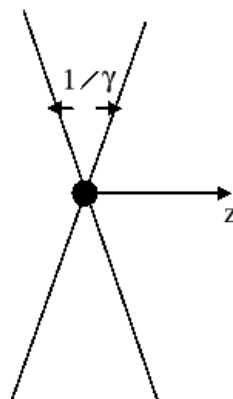
Figure 3.1: *Electric field lines for a relativistic charge.*
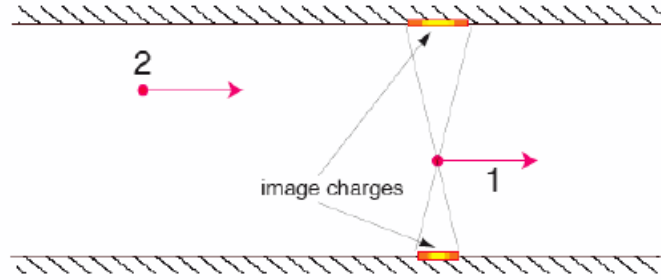
Figure 3.2: *Charge traveling inside a perfectly conducting pipe of arbitrary cross section. Shown are the image charges on the wall generated by the leading charge.*

charge without affecting it nor affecting any trailing charge traveling in front of or behind the leading one.

On the contrary if the conducting wall has a non-vanishing resistivity the situation is different because the image charge moving on the surface of the wall now lag slightly behind the charge :thus both longitudinal and transverse field components are now present.

Considering the more general case of wall discontinuities, that is linac accelerating structures, bellows or complicated vacuum chambers, the charge Q traveling with a velocity close to the speed of light gives rise to a scattered electromagnetic field. These electromagnetic fields , generated in an enclosed space, are called wake fields since, from causality, the leading charge cannot affect itself nor any charge in front of it but only charges lying behind it. We can estimate the distance(catch up distance) at which the electromagnetic field generated by the leading charge reaches the trailing charge, traveling at a distance s, as follow (see fig. 3.3)

$$ct = \sqrt{(z-s)^2 + b^2}$$

$$z^2 = (z-s)^2 + b^2$$
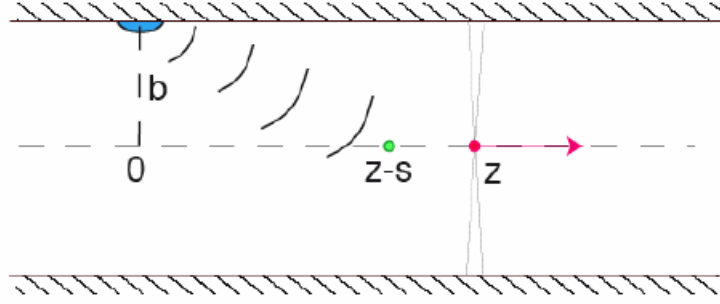
Figure 3.3: *A wall discontinuity located at $z = 0$ scatters the magnetic field generated by an ultra relativistic charge. When the charge is in z the scattered magnetic field reaches $z - s$.*

and if $s \ll b$

$$z_{catchup} = \frac{b^2}{2s} \tag{3.1}$$

In this chapter we briefly recall the general definition of the longitudinal and transverse wake fields. We then apply it to the case of the Spark project, where the cavities geometries and the short bunch length, allow the use of the diffraction model for a single cavity. The diffraction model suppose the electromagnetic field, scattered at the edge of the cavity, is just that of a plane wave; thus it is possible to use the classical diffraction theory of optics to calculate the fields. An asymptotic solution for a periodic collection of cavity is also given.

3.1 Wake Fields and Impedances

When a charge Q travels along the axis of an accelerator structure, the trailing charge q changes its energy under the effect of the longitudinal Lorentz force $F_{\parallel}(s, z)$ produced by the leading charge, [16]

$$U(s) = -\int_{-\infty}^{\infty} \boldsymbol{F}_{\parallel}(s, z) dz \tag{3.2}$$
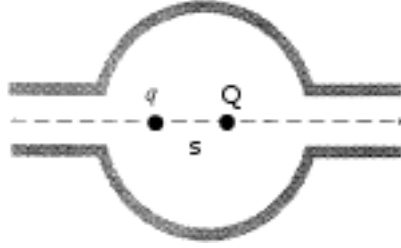
Figure 3.4: *Leading, Q, and trailing, q, charges on the axis z of a symmetric cavity.*

where z is the longitudinal coordinate along the structure, see fig. 3.4.

Using eq. 3.2 the impulsive longitudinal wake potential is defined as

$$W_{||0}(s) = \frac{U(s)}{qQ} \tag{3.3}$$

The impulsive longitudinal wake potential is measured in V/C and it represents the time response of a system to a unit impulse, that is it's a Green function; as a consequence we can calculate the longitudinal wake field of an arbitrary charge distribution Q by applying the superposition principle that is by making the convolution of the bunch distribution with the Green function

$$W_{||}(s) = \frac{1}{Q} \int_{-\infty}^{\infty} \lambda(s - s')W_{||0}(s')ds'$$

where $\lambda(s) = Q/L$ is the longitudinal density of a bunch of length L. For all practical purpose, the impulsive wake potential of relativistic bunches is zero for all negative s

$$W_{||}(s) = \frac{1}{Q} \int_{0}^{\infty} \lambda(s - s')W_{||0}(s')ds' \tag{3.4}$$

Analogously let's consider a leading charge Q traveling transversally displaced with respect to the axis as shown in fig. 3.5.

In this case the leading charge excites electromagnetic fields which give
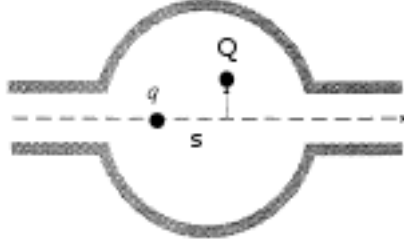
Figure 3.5: *Leading, Q, and trailing, q, charges in a symmetric cavity. The leading charge is transversally displaced.*

rise to a transverse electromagnetic force $F_\perp(s,z)$. The trailing charge, experiencing it, gains a transverse momentum

$$M(s) = \int_{-\infty}^{\infty} \boldsymbol{F}_\perp(s,z)dz \qquad (3.5)$$

Using eq. 3.5 the impulsive transverse wake potential is defined as

$$W_{\perp 0}(s) = \frac{M(s)}{qQx} \qquad (3.6)$$

where x is transverse displacement of the leading charge from the axis of the chamber.

It represents, as in the previous case, the time response of a system to a unit impulse; it's units are V/Cm.

We can use the transverse Green function to obtain the transverse wake field of an arbitrary distribution charge Q of particles

$$W_\perp(s) = \frac{1}{Q} \int_{-\infty}^{\infty} \lambda(s-s')W_{\perp 0}(s')ds' \qquad (3.7)$$

Both the transverse and longitudinal wake field have been obtained in the time domain. Fourier transforming them in the frequency domain we get the spectrum response of the point charge wake function

$$Z_{||}(\omega) = \frac{1}{c} \int_{-\infty}^{\infty} W_{||0}(s)e^{jw\frac{s}{c}}ds \qquad (3.8)$$

54
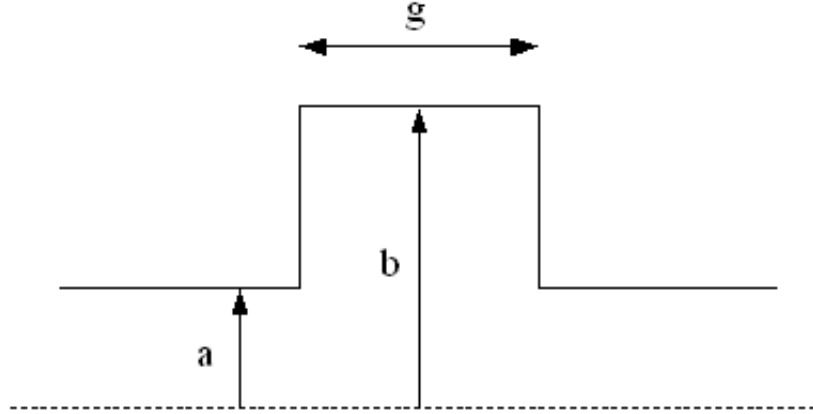
Figure 3.6: *Geometric parameters for a pill box with attached tubes .*

$$Z_\perp(\omega) = -\frac{j}{c} \int_{-\infty}^{\infty} W_{\perp 0}(s) e^{jw\frac{s}{c}} ds \qquad (3.9)$$

3.2   Wake Fields for the SPARC Photo-injector

A bunch traveling off axis across structures whose shape is not uniform, such RF cavity or bellows, generates longitudinal and transverse wake fields as reported in sec. 3.1. The bunch produced in the SPARC photo-injector, see cap. 1, is short enough as respect with the beam pipes connecting RF cavities or bellows; thus the use of a diffraction model, [17] for the wake fields calculation is allowed.

3.2.1   Single cavity: wake fields diffraction model

The wake fields diffraction model suppose each structure as a pill box cavity, whose geometric dimensions are: a the beam pipe radius, b the cavity radius and g its length, see fig. 3.6

When the bunch length σ is much smaller than the beam pipe radius a

$$\sigma \ll a \qquad (3.10)$$

methods of diffraction theory are used to calculate the impedance at high frequencies

$$\omega \gg \frac{c}{a} \tag{3.11}$$

where ω is the angular frequency and c is the speed of light.

When a bunch reaches the edge of the cavity, the electromagnetic field produced is just the one that would occur when a plane wave passes trough a hole; with this hypothesis it is possible to use the classical diffraction theory of optics to calculate the impedance. According to it, the resistive part $R_{||}(\omega)$ of the longitudinal cavity impedance and of the transverse cavity impedance are respectively

$$R_{||}(\omega) = \frac{Z_0}{2\pi^{3/2}} \sqrt{\frac{cg}{a^2}} \omega \tag{3.12}$$

$$R_{\perp}(\omega) = \frac{Z_0 \sqrt{g}}{\pi^{3/2} a^3} \left(\frac{c}{\omega}\right)^{3/2} \tag{3.13}$$

where $Z_0 = 377\Omega$ is the impedance of free space. The wake function is derived from the impedance by inverting the Fourier integral for the longitudinal wake

$$W_{||}(s) = \frac{1}{2\pi} \int_{-\infty}^{\infty} Z_{||}(\omega) e^{j\omega s} d\omega \tag{3.14}$$

and for the transverse wake

$$W_{\perp}(s) = \frac{j}{2\pi} \int_{-\infty}^{\infty} Z_{\perp}(\omega) e^{j\omega s} d\omega \tag{3.15}$$

From eq. 3.12 and eq. 3.13, using the properties of the impedances, we obtain the impulsive longitudinal and transverse wake function respectively

$$W_{||0}(s) = \frac{Z_0 c}{\sqrt{2}\pi^2 a} \sqrt{\frac{g}{s}} \tag{3.16}$$

$$W_{\perp 0}(s) = \frac{2^{3/2} Z_0 c}{\pi^2 a^3} \sqrt{gs} \tag{3.17}$$

56

The above expressions are given for the ultra-relativistic case $\beta \to 1$; the case of low energy regime was studied in [25] and [7] where It was shown a dependence of the energy loss and of the wake fields from the relativistic factor γ. However It was shown in [26] that the high energy regime represents an over estimation of the low energy one.

It's worth noting that both the longitudinal and transverse wakes do not depend on the cavity radius b. The reason is that the diffraction model considers only fields generated at the cavity edge, that is where the beam pipe meets the cavity; part of the diffracted field, generated when the leading edge of the bunch enters the cavity, will propagate in the cavity and if the bunch's rms length σ is shorter than the cavity radius b, then the geometrical condition

$$g < \frac{(b-a)^2}{2\sigma} \tag{3.18}$$

is fulfilled and the scattered field coming from the upper wall of the cavity will never reach the tail of the bunch itself: this is called "cavity regime", [16], [27]. Using eq. 3.16, eq. 3.17 as a green function, eq. 3.4 and eq. 3.7 we can calculate the longitudinal and transverse wake field, inside and outside the bunch, for a bunch of length L whose charge Q is uniformly distributed, we obtain inside the bunch

$$W_{||}(s) = \frac{1}{Q}\int_0^s W_{||0}(s')ds' \tag{3.19}$$

and outside the bunch

$$W_{||}(s) = \frac{1}{Q}\int_{s-L}^s W_{||0}(s')ds' \tag{3.20}$$

Solving eq. 3.19 and eq. 3.20 we obtain

$$W_{||}(s) = \begin{cases} 0 & s < 0 \\ \frac{2}{\sqrt{2}}\frac{Z_0 c}{\pi^2 a L}\sqrt{gs} & 0 < s < L \\ \frac{2}{\sqrt{2}}\frac{Z_0 c}{\pi^2 a L}\sqrt{g}\left(\sqrt{s} - \sqrt{s-L}\right) & s > L \end{cases}$$

Analogously for the transverse wake fields:

$$W_\perp(s) = \frac{1}{Q} \int_0^s W_{\perp 0}(s') ds' \tag{3.21}$$

$$W_\perp(s) = \frac{1}{Q} \int_{s-L}^s W_{\perp 0}(s') ds' \tag{3.22}$$

Solving eq. 3.21 and eq. 3.22 we obtain

$$W_\perp(s) = \begin{cases} 0 & s < 0 \\ \frac{2^{5/2}}{3} \frac{Z_0 c}{\pi^2 a^3 L} \sqrt{g} s^{3/2} & 0 < s < L \\ \frac{2^{5/2}}{3} \frac{Z_0 c}{\pi^2 a^3 L} \sqrt{g} \left(s^{3/2} - (s-L)^{3/2} \right) & s > L \end{cases}$$

3.2.2 Periodic structure: asymptotic wake fields

For a periodic collection of cavity of period p, the asymptotic, longitudinal impedance, at high frequency, is given by [28]

$$Z(k) \approx \frac{j Z_0}{\pi k a^2} \left[1 + (1+j) \frac{\alpha(g/p) p}{a} \left(\frac{\pi}{kg} \right)^{1/2} \right]^{-1} \tag{3.23}$$

with $\alpha(x) \approx 1 - 0.465\sqrt{x} - 0.070 x$. Note that for a periodic structure the real part of the impedance $\Re(Z) \sim k^{(-3/2)}$.

Inverse Fourier transforming the above equation we can obtain the asymptotic longitudinal wake field per cell of for very short range wake field. Anyway using a modal summation technique, it is possible to obtain the wake field numerically, which can be easily fitted to a simple function. The obtained impulsive wake field is valid over a larger range of s and it can be used as a Green function for arbitrary distributions bunch [29]:

$$W_{0\parallel}(s) = \frac{Z_0 c}{\pi a^2} e^{-\sqrt{s/s_1}} \tag{3.24}$$

with

$$s_1 = 0.41 \frac{a^{1.8} g^{1.6}}{p^{2.4}} \tag{3.25}$$

A similar derivation exists for the transverse wake field, which is found to be

$$W_{0\perp}(s) = \frac{4Z_0 c s_2}{\pi a^4} \left[1 - \left(1 + \sqrt{\frac{s}{s_2}} \right) e^{-\sqrt{s/s_2}} \right] \tag{3.26}$$

with

$$s_2 = 0.17 a^{1.79} g^{0.38} / p^{1.17} \tag{3.27}$$

It's worth noting that in this case the longitudinal and transverse impulsive wake field are given in V/Cm and V/Cm^2 respectively, that is their definition is given per cell.

These results are asymptotic, that is they are valid only after the beam has passed a critical number of cells N_{crit}. A qualitative estimation of the number of cell needed for the wake to approach the asymptotic results is given in [30] that is

$$N_{crit} = \frac{a^2}{2g \left(\sigma_z + \frac{2a}{\gamma} \right)} \tag{3.28}$$

where σ_z is the rms length of the bunch, which is quite similar to the numerical estimation given for a Gaussian bunch in [29] when $\gamma \to \infty$

$$N_{crit} = \frac{\alpha a^2}{g \sigma_z} \tag{3.29}$$

where α approaches unity. We uses eq. 3.28 because it was obtained in a more general way.

We can now calculate, as for a single cavity, the longitudinal and transverse wake field for a uniformly charged bunch, of charge Q, and length L. Solving the convolution integrals, eq. 3.19 and eq. 3.20, we obtain for the longitudinal wake field

$$W_{||}(s) = \begin{cases} 0 & s < 0 \\ \frac{2Z_0 c s_1}{\pi a^2 L} \left[1 - e^{-\sqrt{s/s_1}} \left(1 + \sqrt{\frac{s}{s_1}} \right) \right] & 0 < s < L \\ \frac{2Z_0 c s_1}{\pi a^2 L} \left[e^{-\sqrt{\frac{s-L}{s_1}}} \left(1 + \sqrt{\frac{s-L}{s_1}} \right) - e^{\sqrt{\frac{s}{s_1}}} \left(1 + \sqrt{\frac{s}{s_1}} \right) \right] & s > L \end{cases}$$

and using the convolution integrals, eq. 3.21 and eq. 3.22, for the transverse wake field we obtain

$$
W_\perp(s) = \begin{cases}
0 & s < 0 \\[2mm]
\frac{4Z_0 c s_2{}^2}{\pi a^4 L}\left[-6 + \frac{s}{s_2} + 2e^{-\sqrt{\frac{s}{s_2}}}\left(3 + 3\sqrt{\frac{s}{s_2}} + \frac{s}{s_2}\right)\right] & 0 < s < L \\[2mm]
\frac{4Z_0 c s_2{}^2}{\pi a^4 L}\left\{\frac{L}{s_2} + 2\left[e^{-\sqrt{\frac{s}{s_2}}}\left(3 + 3\sqrt{\frac{s}{s_2}} + \frac{s}{s_2}\right) + \right. \right. \\[2mm]
\left. \left. + e^{-\sqrt{\frac{s-L}{s_2}}}\left(-3 - 3\sqrt{\frac{s-L}{s_2}} - \frac{s-L}{s_2}\right)\right]\right\} & s > L
\end{cases}
$$

Chapter 4

Beam Dynamics in Homdyn

Homdyn is a semi-analytical code, developed to describe the dynamics of charged particles beams moving along accelerators devices.

The simulation of a bunch moving, for example, from the photo-injector of a FEL project trough the linac to the entrance of an undulator, involves non linear forces; thus multi-particle codes, such as Parmela, requires several hours of CPU time to run. On the contrary Homdyn, being a semi-analytical code, is very fast.

The main approximation of the Homdyn code lie in the assumption a uniformly charged cylinder represents the bunch. The cylinder is divided in an array of cylinders; the dynamics of each slice is described by differential equations for the envelope and for the centroids. Each slice cannot change its charge, anyway, for it is subject to the local field, the cylinders can change their lengths, radius and angle with respect to the axis; using such information the energy spread and the emittance degradation can be calculated.

The basic optical equation, which describes the motion of particles, is known as the paraxial ray equation. The paraxial ray equation is a second order differential equation in which the angle between the particle trajectories and the axis is assumed small: this means the paraxial ray equation specifies the trajectory in the neighborhood of the axis and also that the fields, actually
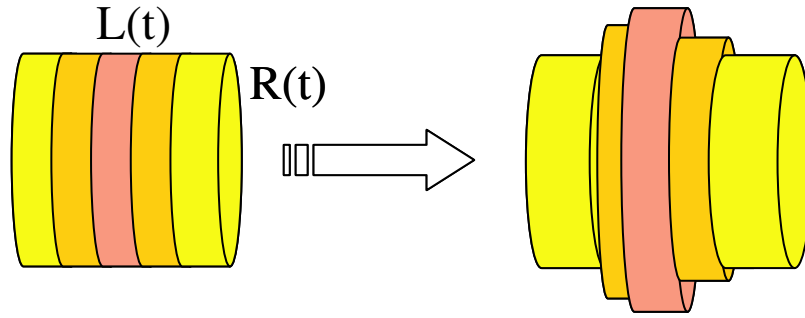
Figure 4.1: *The Multi-slice approximation of the Homdyn bunch.*

experienced by the particles, are expressed as first order expansions of the fields on the axis. As a consequence the axial field components are essentially independent of r and radial components are proportional to r, being r the radial distance from the axis. A paraxial ray equation calculated on the radius R of the bunch is known as envelope equation.

In this chapter we introduce the envelope equation used in the Homdyn code to describe the dynamics of a bunch traveling on axis: the emittance force and the space charge force for a finite length bunch uniformly charged are included in the envelope equation.

The bunch is supposed to travel off axis; in this case to describe the displacement of the bunch from the nominal axis it is necessary to introduce in the code the differential equations for the centroid motion of each slice.

A bunch traveling off axis across structures whose shape is not uniform experiences transverse wake fields; thus the longitudinal and transverse wake fields are introduced in the differential equation.

The equations contain the space charge on the slice centroids generated by the neighbor slices.

Besides the beam can move in a solenoid field; the solenoid coils misalignment with respect to the nominal axis is included. To validate the models adopted in Homdyn for the space charge on centroids we compared Homdyn's results with the well known code Parmela. Finally we show the emittance

analytical computation used in the Homdyn code.

4.1 On-axis beam Dynamics in Homdyn

The motion of a particle due to the Lorentz force

$$\boldsymbol{F} = e(\boldsymbol{E} + \boldsymbol{v} \times \boldsymbol{B}) \tag{4.1}$$

is determined by Newton's equation

$$\frac{d\boldsymbol{P}}{dt} = \boldsymbol{F} = e(\boldsymbol{E} + \boldsymbol{v} \times \boldsymbol{B}) \tag{4.2}$$

The paraxial ray equation can be deduced from eq. 4.2. As mentioned above the assumption is that the particle's trajectories remains near the axis. We obtain [5], [6]

$$r'' + \frac{\gamma'}{\gamma\beta^2}r' + \left(\frac{eB_z}{2mc\beta\gamma}\right)^2 r = 0 \tag{4.3}$$

The second term on the left hand side contributes to the decrease of the angle the particle form with the axis, as the particle accelerates. The fourth term represents a magnetic focusing effect, being B_z the on axis magnetic field.

4.1.1 Space charge and emittance pressure

Let's consider an infinite cylindrical bunch. From eq. 4.3 we can deduce the envelope equation for an on-axis beam: we substitute the envelope R to r and we add two other effects: the space charge force, which includes both the electric and the magnetic field, and the emittance force.

Concerning the space charge force, we can use again eq. 4.2 for the transverse motion

$$\frac{d(\gamma m dR/dt)}{dt} = e(E_r + (\boldsymbol{v} \times \boldsymbol{B})_r) = e(1 - \beta^2)E_r = \frac{eE_r}{\gamma^2} \tag{4.4}$$

The space charge electric field for an infinite uniformly charged cylinder was obtained in sec. 2.1, thus substituting eq. 2.2 to E_r we obtain, for the only space charge force,

$$\frac{d^2(\gamma m R)}{dt^2} = \frac{e I_0}{2\pi\epsilon_0\beta c\gamma^2}\frac{1}{R} \tag{4.5}$$

where $I_0 = 4\pi\epsilon_0 mc^3/e \approx 17kA$ is the Alven current.

A beam with a non zero emittance expands; in order to obtain an expression for the emittance, we can view nonzero emittance in terms of an outward force that balances the focusing force to maintain a constant radius beam. In the hypothesis the beam is cylindrical and paraxial, we write the linear focusing force as

$$F_r(r) = -F_0(r/R) \tag{4.6}$$

thus

$$\ddot{r} + \frac{F_0}{\gamma m R}r = 0 \tag{4.7}$$

The orbit vector points of individual particles follow ellipses in trace space as the particles perform radial oscillations. The oscillation frequency for all particles is

$$\omega_r = \sqrt{F_0/\gamma m R} \tag{4.8}$$

The radial emittance is at the waste, by definition (see cap. 1)

$$\epsilon_r = RR' = \omega_r R^2/\beta c \tag{4.9}$$

Solving for the oscillation frequency, we obtain

$$\omega_r = \epsilon_r\beta c/R^2 \tag{4.10}$$

Equating eq. 4.8 and eq. 4.10 we obtain the focusing force needed to balance emittance on the envelope. This can be included in eq. 4.5

$$\frac{d^2(\gamma m R)}{dt^2} = \frac{\epsilon_r^2 \gamma m (\beta c)^2}{R^3} + \frac{eI_0}{2\pi\epsilon_0 \beta c \gamma^2} \frac{1}{R} \tag{4.11}$$

It's worth noting that unlike the first three terms inserted in the paraxial equation, the space charge force and the emittance force are defocusing forces induced by the self field of the bunch, see fig. 4.2

Using the rule

$$\dot{R} = \frac{dR}{dt} = R'\beta c \tag{4.12}$$

we can now write the complete envelope equation, where $'$ is the space derivative d/dz as

$$R'' + \frac{\gamma'}{\gamma\beta^2}R' + (\frac{eB_z}{2mc\beta\gamma})^2 R = \frac{K}{R} + \frac{\epsilon^2}{R^3} \tag{4.13}$$

where

$$K = \frac{eI_0}{2\pi\epsilon_0 m(\beta\gamma c)^3} \tag{4.14}$$

The ratio ρ, see sec. **??**, of the space charge force upon the emittance force

$$\sigma = \frac{\epsilon^2}{KR^2} \tag{4.15}$$

describes a thermal or a laminar beam: when ρ is greater than one the beam is called laminar otherwise it is thermal.

The envelope equation used in Homdyn is written in terms of the envelope time derivative and it describes the dynamics of a finite length bunch shaped as a uniformly charged cylinder; the electric field used in the envelope equation is the one obtained in sec. 2.2 for a bunch of length L and charge Q:

$$\ddot{R} + \beta\gamma^2\dot{\beta}\dot{R} = \frac{e}{m\gamma^3}E_r(\xi_s) + \left(\frac{4\epsilon^t h_n c}{\gamma}\right)^2 \frac{1}{R^3} \tag{4.16}$$
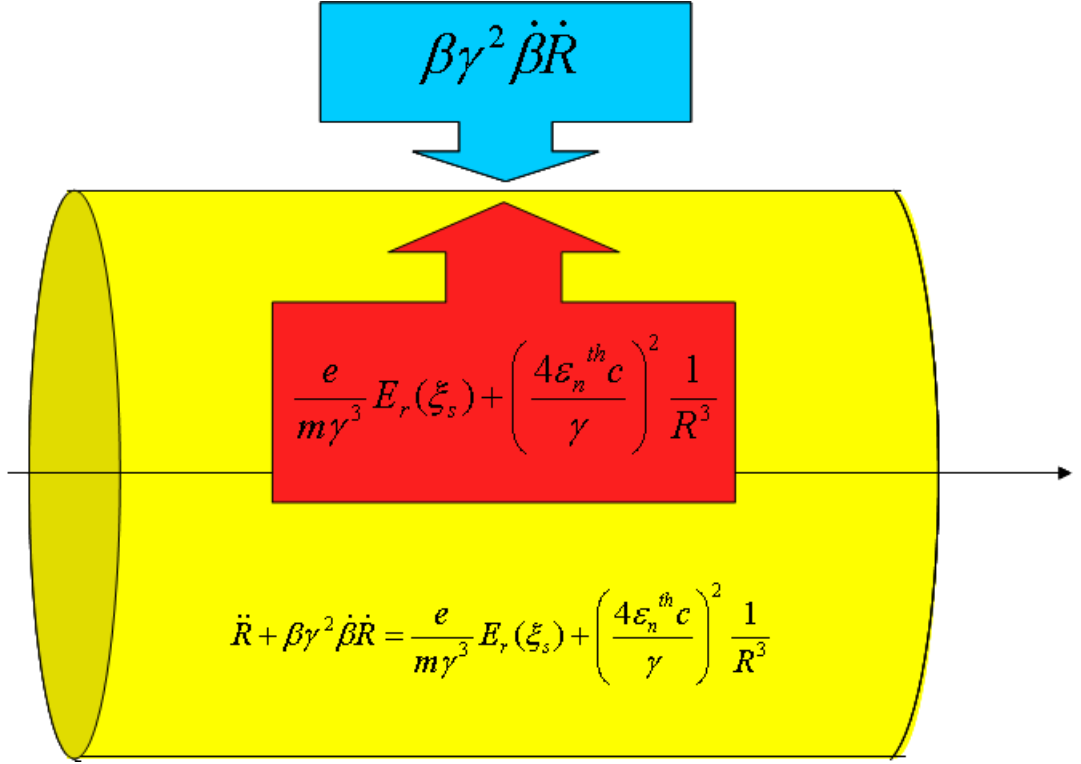
Figure 4.2: *Schematic view of the envelope equation.*

that is [11]

$$\ddot{R} + \beta\gamma^2\dot{\beta}\dot{R} = \frac{e}{m\gamma^3}\frac{Q\gamma}{4\pi\epsilon LR}\left[\frac{L-\xi_s}{\sqrt{\gamma^2(L-\xi_s)^2 + R^2}} + \frac{\xi_s}{\sqrt{\gamma^2\xi_s^2 + R^2}}\right] +$$

$$+ \left(\frac{4\epsilon^{th_n}c}{\gamma}\right)^2\frac{1}{R^3} \quad (4.17)$$

where $\xi_s = z_s - z_t$, z_t is the considered slice's tail and z_s represents any position along the slice. Fig. 4.2 shows a schematic view of the envelope equation.

From the Newton's equation, eq. 4.2, we write the bunch's longitudinal motion

$$\ddot{z}_c = \dot{\beta}c$$

$$\dot{\beta}_s = \frac{e}{mc\gamma^3}(E_z(\xi_s) + E_z^{RF})$$

66

that is

$$\ddot{z}_c = \frac{e}{m\gamma^3} \left\{ \frac{Q}{2\pi\epsilon R^2 L\gamma} \right.$$
$$\left. \left[\gamma(|\xi_s| - |L - \xi_s|) + \sqrt{\gamma^2(L - \xi_s)^2 + R^2} - \sqrt{\gamma^2\xi_s^2 + R^2} \right] + E_z^{RF} \right\} \quad (4.18)$$

where z_c is the slice centroid longitudinal position, E_z^{RF} is the accelerating field, induced by RF cavities and $E_z(\xi_s)$ the longitudinal space charge generated by a finite cylinder uniformly charged. The Homdyn code uses the differential equation showed above, eq. 4.17 and eq. 4.18, to describe each slice evolution along the accelerator structures.

4.2 Off-axis Beam Dynamics in Homdyn

4.2.1 Longitudinal and Transverse Wake Field

Let's consider now a bunch traveling across structures whose shape is not uniform. As seen in Cap. 3, the bunch induces electromagnetic fields which act back on the bunch itself: these fields, acting behind the bunch's head, are called wake fields. When the bunch travels on the structures' axis, it generates only longitudinal wake fields; we can introduce the longitudinal wake fields in eq. 4.18, obtaining

$$\ddot{z}_c = \frac{e}{m\gamma^3}(E_z(\xi_s) + E_z^{RF}) + \frac{e}{\gamma m}E_{||}(\xi_s) \quad (4.19)$$

where $E_{||}$ is longitudinal wake field obtained in sec. 3.2 for cavity or a periodic array of cavities.

Of course, if the bunch is traveling on axis the slice centroids x_c don't experience any transverse motion. Anyway, due to lasers jitters pointing instability or misalignments, a bunch can be travel slightly off axis and when a bunch's travels along an accelerating structures, transverse time depen-
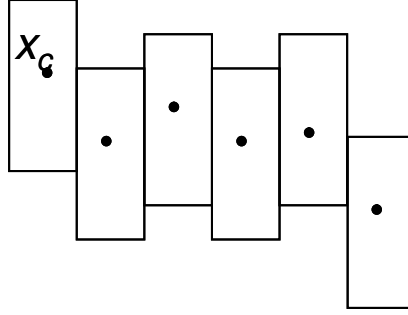
Figure 4.3: *Off axis bunch.*

dent fields, such as transverse RF components, may induce correlated slice centroids displacement as in fig. 4.3.

In these cases, in order to describe the displacement of each slice centroid x_c and y_c from the nominal axis of the bunch, it is necessary to include in the code the differential equation describing the centroid motion [13], [14].

Such equations contain the transverse wake fields. It considers the wake fields as produced by the sum of the wake fields generated by each slice; the displacement is related to the displacement of each slice. The former includes only the displacement of the first slice thus it's an approximation, on the contrary the latter doesn't contain any approximation but the Homdyn code is a little bit slower to run because it obtains the wake fields as the sum of the wake fields produced by the single slices.

The Homdyn differential equation describing each slice's centroid transverse motion, including only the wake fields, is

$$\ddot{x}_c + \beta\gamma^2\dot{\beta}\dot{x}_c = \frac{e}{\gamma m}\sum_{s=1}^{S} E_\perp(x_{cs}, \xi_s) \tag{4.20}$$

where s is index over the S slices.
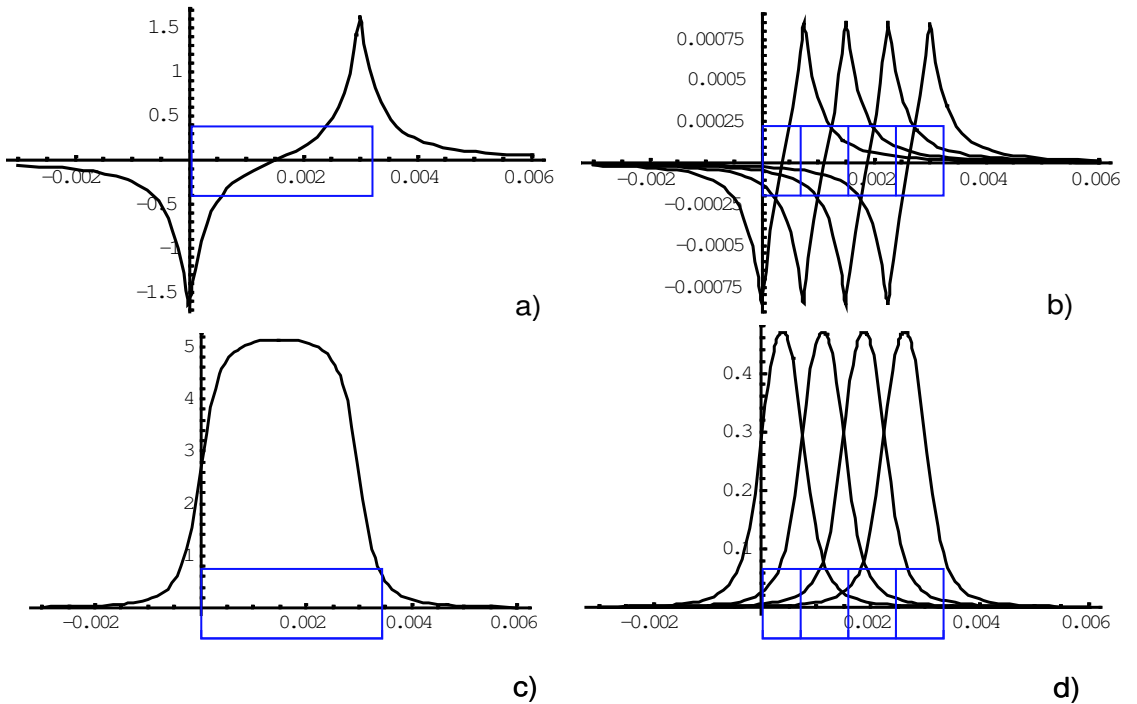
The same equations holds for y_c.

Figure 4.4: *Longitudinal, (a) and (b), and transverse, (c) and (d), space charge electric field, generated by the whole bunch, (a) and (c), and as superposition of the single slice electric field, (b) and (d).*

4.2.2 Space Charge

When each slice's centroid is transversally displaced from the nominal axis, it also experiences a transverse deflection due to the space charge force produced by the neighbor slices [13], [14]. As for the wake fields, we can use two different approaches to obtain the space charge field: in the first approach the whole bunch generates the space charge, see fig. 4.4 (a) and (c), whilst in the second the single slices generates the space charge, see fig. 4.4 (b) and (d).

The first approach supposes the space charge on centroids varies linearly with the distance d_{xc} of the considered slice's centroid from a straight line r.

The straight line r is obtained interpolating the centroids along the bunch with the least square method, see fig. 4.5, and the longitudinal and transverse
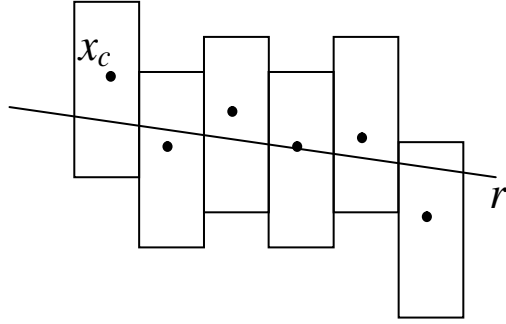
Figure 4.5: *Interpolating straight line for bunch centroids displacement.*
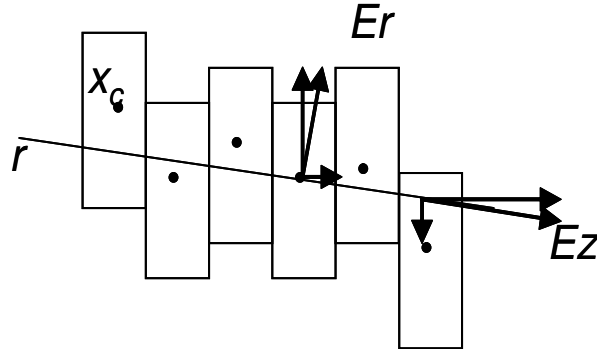
Figure 4.6: *Space charge electric field projections along and perpendicular to the longitudinal axis z.*

space charge electric field are obtained as the projection of the longitudinal and radial electric field with respect the new bunch's axis r as shown in fig. 4.6.

Following the first approach the centroid transverse motion due to space charge is

$$\ddot{x}_c + \beta\gamma^2\dot{\beta}\dot{x}_c = \frac{e}{m\gamma^3}[E_z(\xi_s)sin\theta - E_r(\xi_s, d_{xc})cos\theta] \tag{4.21}$$

and the longitudinal motion is described by

$$\ddot{z}_c = \frac{e}{m\gamma^3}[E_z(\xi_s)cos\theta - E_r(\xi_s, d_{xc})sin\theta] \tag{4.22}$$

The longitudinal electric field remains unchanged (see eq. 2.6)

$$E_z(\xi_s) = \frac{Q}{2\pi\epsilon R^2 L\gamma} \left[\gamma(|\xi_s| - |L - \xi_s|) + \sqrt{\gamma^2(L - \xi_s)^2 + R^2} - \sqrt{\gamma^2\xi_s^2 + R^2}\right]$$

(4.23)

whilst the transverse electric field contains the linear dependence on d_{xc}

$$E_r(\xi_s, d_{xc}) = \frac{Q\gamma d_{xc}}{4\pi\epsilon L R^2} \left[\frac{L - \xi_s}{\sqrt{\gamma^2(L - \xi_s)^2 + R^2}} + \frac{\xi_s}{\sqrt{\gamma^2\xi_s^2 + R^2}}\right]$$

(4.24)

In the second approach the space charge is obtained as the sum of the fields of the single slices

$$\ddot{x}_c + \beta\gamma^2\dot{\beta}\dot{x}_c = \frac{e}{m\gamma^3} \sum_{s=1}^{S} E_r(\xi_s, x_c - x_{cs})$$

(4.25)

being

$$E_r(\xi_s, x_c - x_{cs}) = \frac{Q\gamma(x_c - x_{cs})}{4\pi\epsilon L R^2} \left[\frac{L - \xi_s}{\sqrt{\gamma^2(L - \xi_s)^2 + R^2}} + \frac{\xi_s}{\sqrt{\gamma^2\xi_s^2 + R^2}}\right]$$ (4.26)

where E_r simply varies linearly with the distance $x_c - x_{cs}$ of the generating slice, x_{cs}, from the considered slice, x_c.

The longitudinal equation of motion is:

$$\ddot{z}_c = \frac{e}{m\gamma^3} \sum_{s=1}^{S} E_z(\xi_s)$$

(4.27)

where E_z remains unchanged.

As for the wake fields, the main difference concerning the two approaches consists in the CPU run time of the Homdyn code, which remains anyway very low.

4.2.3   Solenoid Magnetic Field

Finally the Homdyn code contains the beam motion in a solenoid field, which was mention previously among the focusing effects. The solenoid magnetic field, obtained as the sum of each coil field, is shown in fig. 4.7.
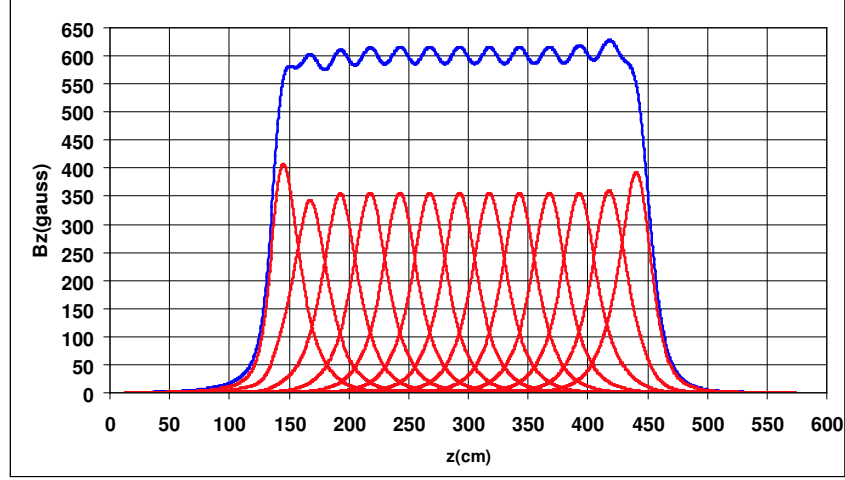
Figure 4.7: *Solenoid field B_z, generated as the sum of the single solenoid coil*

The code includes the case the solenoids coils are misaligned: the following differential equations describes the centroid's transverse and longitudinal motion when solenoid coils are present

$$\ddot{x}_c = \frac{e}{\gamma m}(\dot{y}_c B_z - \dot{z}_c B_y) = \frac{e}{\gamma m}\left[\dot{y}_c + \frac{1}{2}\dot{z}_c\left(y_c B'_z - \sum_i y_{i,off} B'_{z,i}\right)\right]$$

$$\ddot{y}_c = \frac{e}{\gamma m}(\dot{z}_c B_z - \dot{x}_c B_y) = -\frac{e}{\gamma m}\left[\dot{x}_c + \frac{1}{2}\dot{z}_c\left(x_c B'_z - \sum_i x_{i,off} B'_{z,i}\right)\right]$$

$$\ddot{z}_c = \frac{e}{\gamma m}(\dot{x}_c B_z - \dot{y}_c B_y) = -\frac{e}{2\gamma m}\left[\dot{x}_c\left(y_c B'_z - \sum_i y_{i,off} B'_{z,i}\right) + \right.$$
$$\left. - \dot{y}_c\left(x_c B'_z - \sum_i x_{i,off} B'_{z,i}\right)\right]$$

where

$$B_{x,i} = -\frac{1}{2}\frac{dB_{z,i}}{dz}(x_c - x_{i,off}) \qquad (4.28)$$
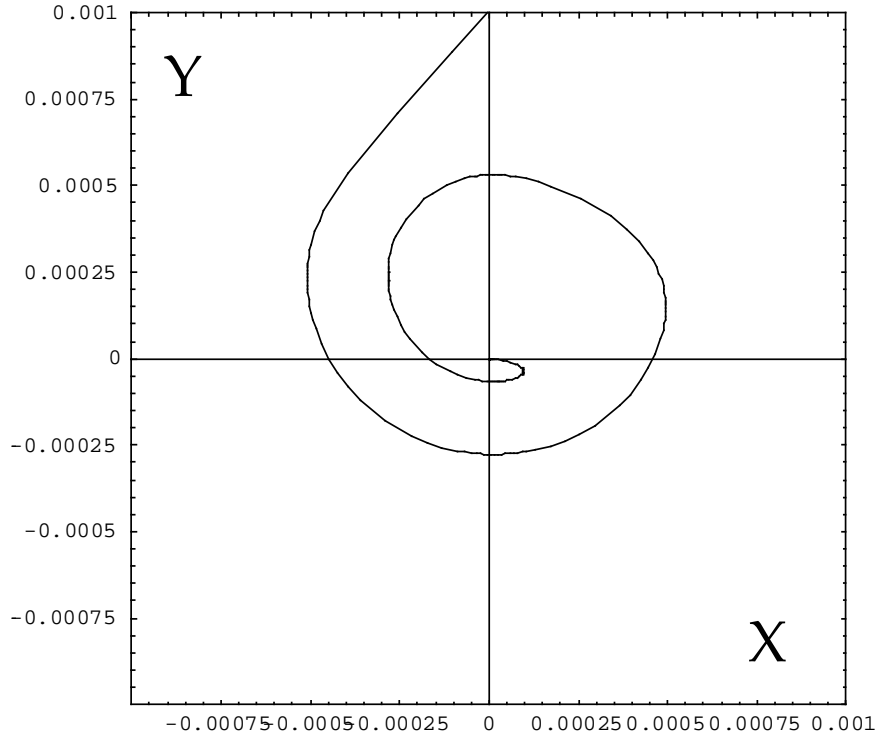
Figure 4.8: *Bunch centroid motion, as computed by Homdyn, in a solenoid field.*

$$B_{y,i} = -\frac{1}{2}\frac{dB_{z,i}}{dz}(y_c - y_{i,off}) \qquad (4.29)$$

being $x_{i,off}$ and $y_{i,off}$ the displacement of the coil i from the nominal axis.

It's worth noting the equation describing the x_c, y_c and z_c motion are coupled. Fig. 4.8 describes the centroid motion in a solenoid field, as computed by Homdyn.

4.2.4 Validation

We test the models adopted in Homdyn to describe the space charge on centroids, using the Parmela code. In particular we generate a bunch whose

Figure 4.9: *Slices' centroids lying on a bent axis.*

slices lies on a bent axis as in fig. 4.9; in this case space charge on centroids is stronger.

Fig. 4.10 show the centroids' evolution along the z axis, as computed by Parmela and Homdyn, when the only space charge force is acting.

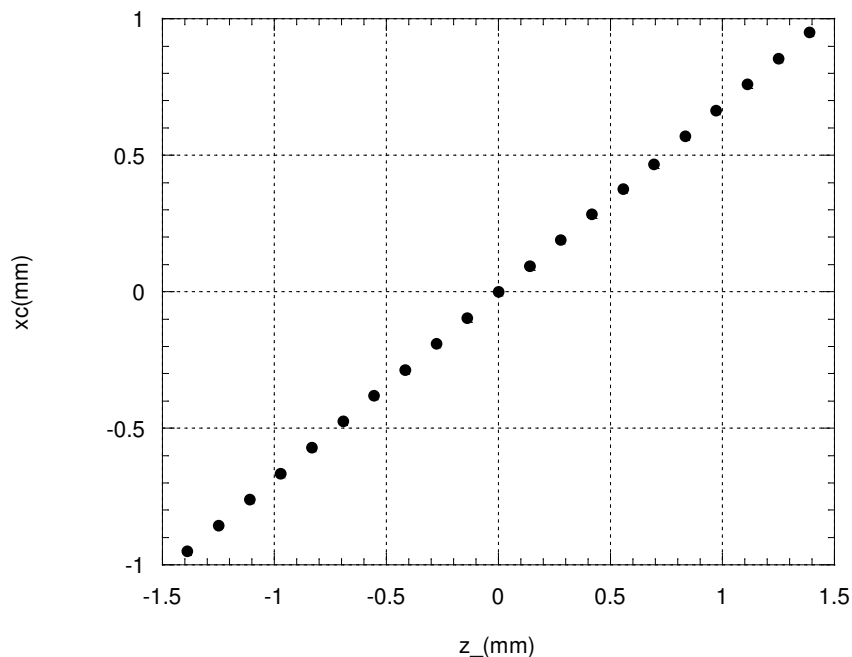The cross represents the first approach whilst the square represents the second one; Parmela is the full circle. It's worth noting there's a good agreement between the two models, anyway in the first case the space charge depends on the distance d_{xc} of each centroid from the interpolating straight line r so as long as the only space charge is affecting the bunch, $d_{xc} = 0$ and we only observe a lengthening effect due to the longitudinal space charge. On the contrary, in the second approach, the distance $x_c - x_{cs}$ of the considered slice from the neighbor slices generating the space charge is not zero; thus the radial space charge is not zero, even if quite small being the chosen tilt angle small. The radial space charge depends on the sign of the distance d_{xc} and it has the effect of transforming the straight line r into a bent line. In
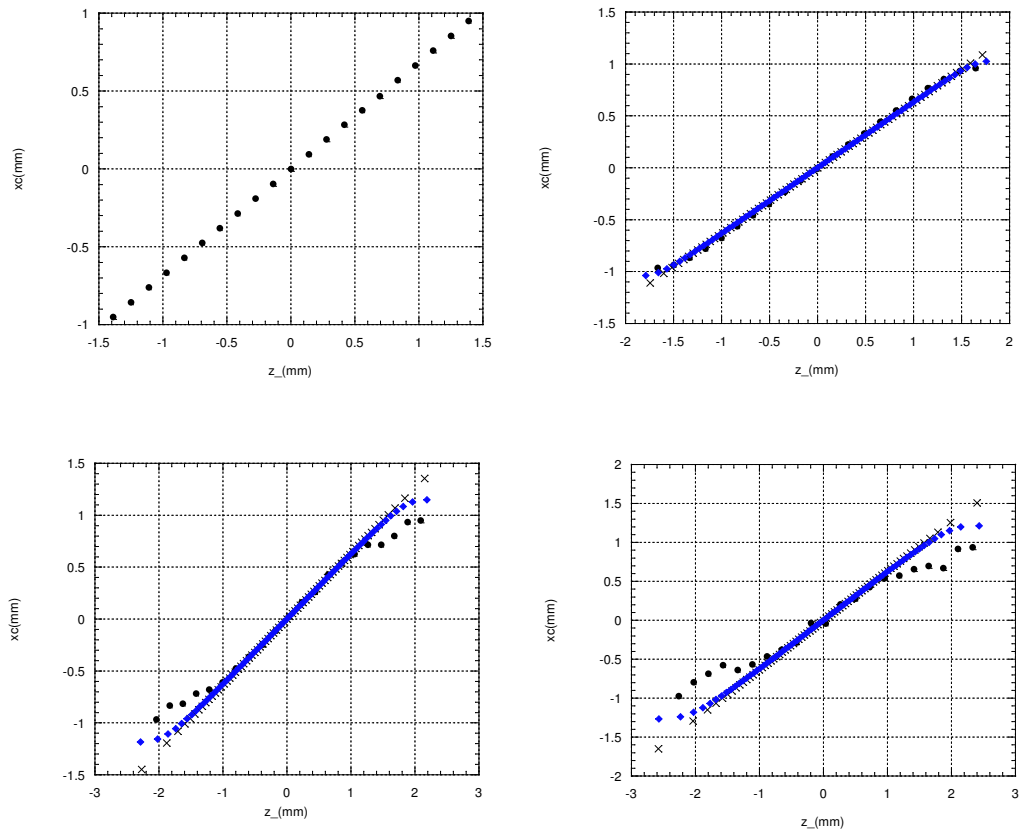
Figure 4.10: *Centroids' evolution along the z axis (from left to right z = 0cm, z = 100cm, z = 200cm and z = 250cm) for Parmela (full circle), first (cross) and second (square) approach for Homdyn .*

Parmela the bending effect is stronger, this is caused by space charge non linearities.

4.3 Emittance Computation

The total rms normalized emittance is calculated in the code following the definition given in sec. **??**

$$\epsilon_{xn}^2 = \big(< (x- < x >)^2 >< (\beta\gamma x'- < \beta\gamma x' >)^2 > +$$
$$- < (x- < x >)(\beta\gamma x'- < \beta\gamma x' >) >^2\big) \quad (4.30)$$

The bunch is divided in S cylindrical slices, uniformly charged and each slice contains M particles. The whole bunch contains $N = S \cdot M$ particles; thus the media $<>$ can be expanded in the following way:

$$<>= \frac{1}{N}\sum_{n=1}^{N} = \frac{1}{S \cdot M}\sum_{s=1}^{S}\sum_{m=1}^{M} = \frac{1}{S}\sum_{s=1}^{S} <>_s \quad (4.31)$$

Besides for a uniform cylindrical charge distribution, the following relation holds:

$$< x^2 >_s= \frac{X_s^2}{4} \quad (4.32)$$

The total rms emittance is calculated in the code as follow

$$\epsilon_{ntot}^2 = \left(\epsilon_n^{th}\right)^2 + (\epsilon_n^{corr})^2 \quad (4.33)$$

where ϵ_n^{th} is the thermal emittance. When all the slices lies on the same axis, the correlated emittance ϵ_n^{corr} is only given by the 'envelope' emittance

$$(\epsilon_n^e)^2 =< \frac{X^2}{4} >< \frac{p_X^2}{4} > - < \frac{Xp_X}{4} >^2 \quad (4.34)$$

where X is the slice envelope and $p_X = \beta\gamma X'$ is the transverse momentum. On the contrary if the slices do not lie on the same axis then the correlated

emittance is not simply given by the envelope emittance but it is given by the quadratic sum of three terms: the envelope emittance, eq. 4.34, the centroids

$$\left(\epsilon_n^{cent}\right)^2 = <(x_c - <x_c>)^2><(p_xc - <p_xc>)^2> +$$
$$- <(x_c - <x_c>)(p_xc - <p_xc>)>^2$$

and the cross emittance, respectively

$$\left(\epsilon_n^{cross}\right)^2 = <\frac{X^2}{4}><(x_c - <x_c>)^2> + <\frac{p_X^2}{4}><(p_xc - <p_xc>)^2> +$$
$$- 2 <\frac{Xp_X}{4}><(x_c - <x_c>)(p_xc - <p_xc>)>$$

The emittance complete expression of an off axis bunch has been inserted in the Homdyn code. We used the Parmela code to validate the emittance computation described above. We run Parmela for simple cases, for example a bunch generated on a photo-cathode with and without laser jitter and space charge. The obtained results for the envelope, centroids positions, envelope and centroids momentum are inserted in the above equations the envelope, the cross and the centroid emittance: then we compare the analytical results with the emittance as computed by Parmela.

Fig. 4.11 compares the total emittance to the Parmela emittance. In fig. 4.11 (a) and (b) the space charge is off whilst it is on in fig. 4.11 (c) and (d). Fig. 4.11 (a) shows the emittance computation when the bunch is traveling on axis: in this case the centroid and cross emittance are equals to zero and Homdyn simply uses the envelope emittance. It's worth noting fig. 4.11 (a) shows the calculation is right. Fig. 4.11 (b) shows the emittance computation when the bunch is traveling off axis. In this case, all the emittances are different from zero. Again fig. 4.11 (b) demonstrates the agreement is excellent thus validating the emittance computation used in Homdyn.

Finally fig. 4.11 (c) and (d) compare the emittance when the space charge is on and when both the bunch is on axis or off axis. The agreement is still
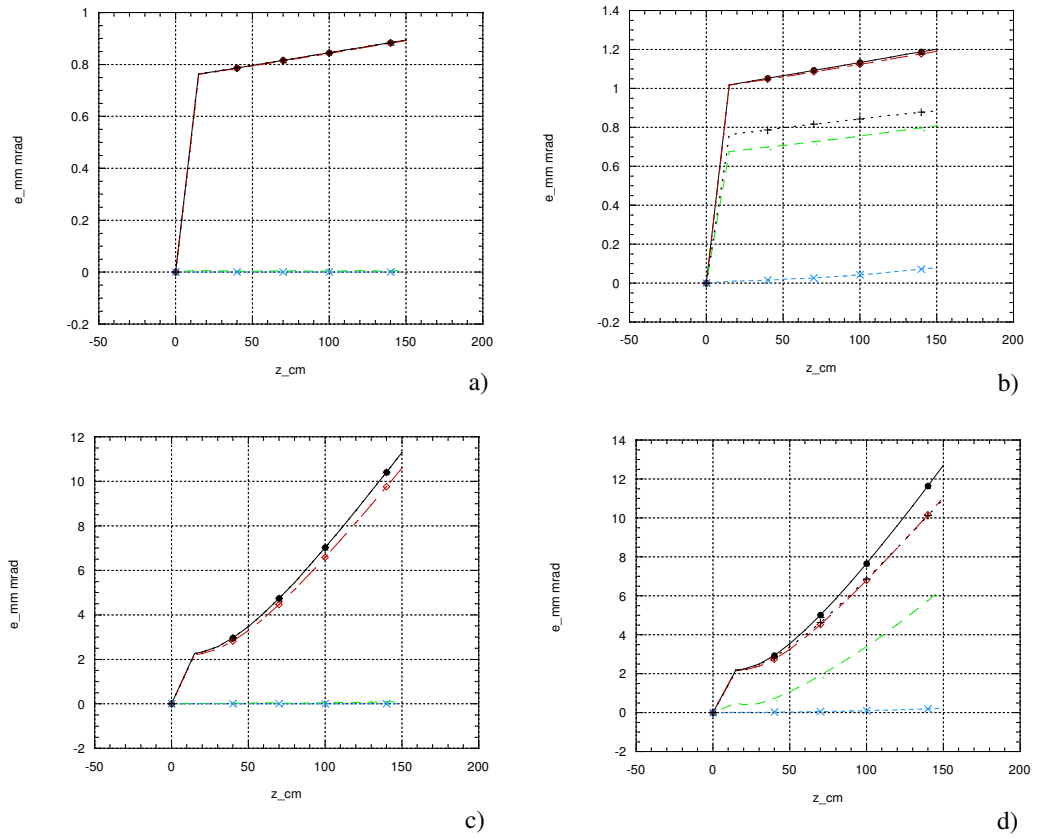
Figure 4.11: *Total (full circle), Parmela (rhombus), cross (dashed line), centroid (times), envelope (cross) emittance when the space charge is off (a and b) and the space charge is on (c and d) with (b and d) without (a and c) offset.*

good: they don't coincide perfectly because the Homdyn emittance calcula-tion assume the bunch's charge distribution uniform. Anyway the good result demonstrates the non linearities of the space charge force can be neglected.

Chapter 5

Emittance Degradation Study in the SPARC photoinjector

The Homdyn code, including its improvement on off axis beam dynamics, has been used in the SPARC project, together with other codes, to study the bunch quality along the photo-injector until the entrance of the undulator device.

In this chapter we analyze emittance degradation due to misalignments along the photo-injector. Infact when a bunch travels off axis, because the bunch is generated off axis or the structure is misaligned, transverse wake fields exist as well and influence the bunch itself.

As a first application of the Homdyn code to the SPARC photo injector we study the emittance and energy spread degradation in the emittance meter experiment. The emittance meter experiment's aim is to measure, with a pepper pot, the emittance just outside the gun to guarantee the bunch enters the linac with the required features. Anyway the bunch's emittance can be degraded by the bellows preceding the pepper pot giving a false measure. Analysis of the bunch quality before the pepper pot has been done with Homdyn including off axis beam dynamics. The Homdyn results for different emittance meter geometries led to the choice of a certain geometries and show the bunch's emittance degradation is negligible.

Moreover we study a correction scheme for the SPARC project to control the bunch's trajectory and angle at the entrance of the undulator. The correction scheme consists of a number of steering magnets and beam position monitors placed along the photo-injector; we tested its validity by the study of a configuration which causes the bunch's centroid going further from the nominal axis thus generating stronger transverse wake fields. Two different steering approaches are analyzed and the emittance degradation is studied. The code demonstrates the steerings positions and number do correct the bunch's orbit and angle and give good results concerning the emittance degradation.

5.1 The Emittance meter experiment: emittance and energy spread degradation

Preliminary studies of the the SPARC RF-Gun are planned to obtain an accurate analysis and optimization of the emittance compensation scheme, measuring the beam emittance evolution downstream the RF-Gun with an appropriate diagnostic system. Since the beam before the accelerating structures is still space charge dominated, the pepper-pot method is used [18]. A pepper-pot consists in a multi-slit mask intercepting the beam; it selects one or several beamlets reducing the dominated space charge incoming beam into some emittance-dominated beamlets that drift up to an intercepting screen as illustrated in fig. 5.1.

The use of a double slit, horizontal and vertical, allows the measure of the emittance and Twiss parameters in both plane. The pepper pot is preceded by a bellow structure , as in fig. 5.2, which allows the pepper pot to move along the nominal axis z and thus it gives the possibility to perform measurements from about $z = 83cm$ to $z = 233cm$.

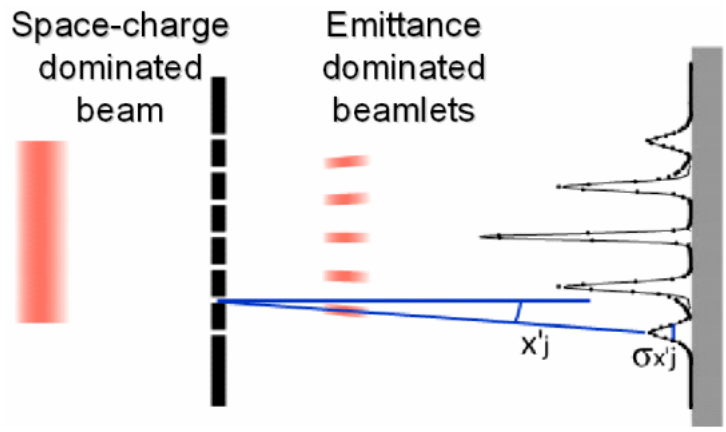An array of cavities constitute the bellow's corrugation. Even if each

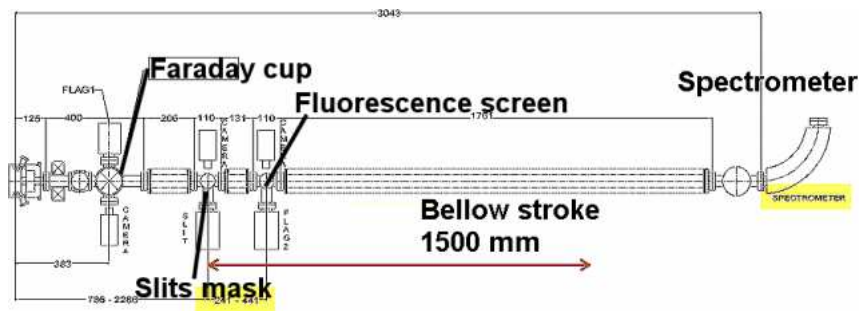Figure 5.1: *The Multi-slits mask intercepting a space charge dominated beam.*

Figure 5.2: *Emittance-meter design.*

corrugation's shape is triangular, we suppose them as squared cavities. This assumption (cap. 3)and the geometric dimensions of the pill-box cavity with respect to the bunch length (see eq. 3.10) allows the use of the diffraction theory model for the calculation of the wake fields in Homdyn.

Tab. 5.1 shows the two bellows configurations for the emittance-meter experiment, where a is the beam pipe radius, b the cavity depth and g its length. The second choice, being its geometric dimensions bigger than the first choice, generates lower wake fields. Anyway, as it will be shown later on, the first choice was adopted for the emittance meter experiment being the resulting emittance degradation negligible.

Bellow	a mm	b mm	g mm
first	26.0	47.5	3.40
second	51.25	75.0	4.00

Table 5.1: The two bellows geometries for the emittance meter experiment.

The plots in fig. 5.3 and fig. 5.4 represents the transverse and longitudinal loss factors as a function of the corrugations' number for a triangular and squared corrugation for the first and second choice respectively. The results calculated with the code ABCI demonstrate the assumption of a pill box cavity for the bellows corrugations give a worst result in terms of wake fields, that is the choice is conservative.

The graph in fig. 5.5 shows the variation in percent of the beam emittance at position $z = 150cm$ from the cathode, due to a bellow misalignment for different values of the beam transverse position with respect to the bellow axis. In the worst case of $1mm$ misalignment the contribution of the wakes to the emittance degradation is lower than 2% thus negligible.

The increasing of the energy spread of the bunch due to longitudinal wake fields trough the long bellows is analyzed in the plot of fig. 5.6. As for the emittance, the degradation of the beam has not practical relevance.

Figure 5.3: *Longitudinal (left hand side) and transverse loss factor for a triangular (full circles) and squared cavity as computed by the ABCI code for the first bellow choice.*
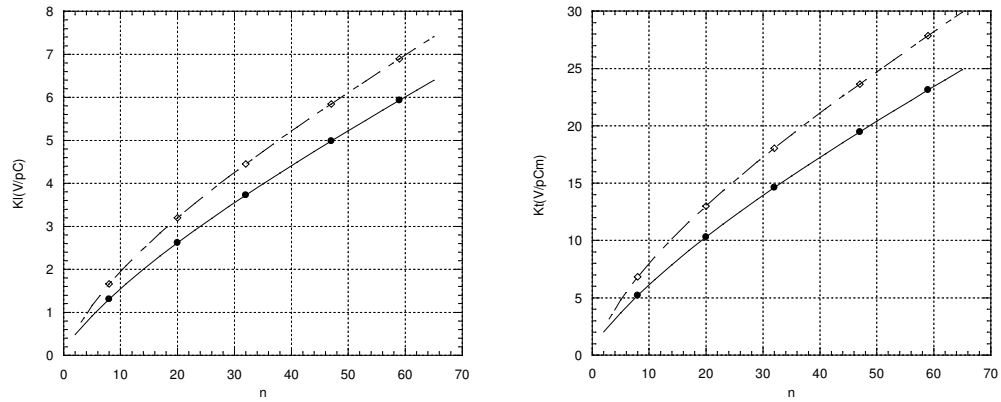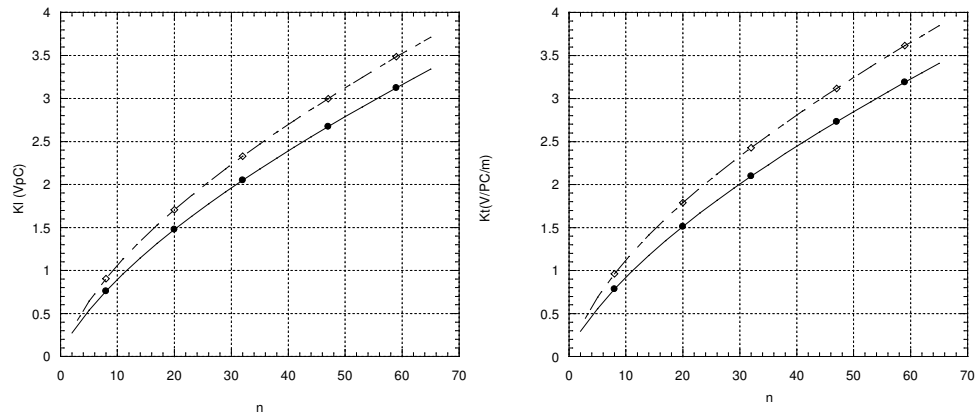

Figure 5.4: *Longitudinal (left hand side) and transverse loss factor for a triangular (full circles) and squared cavity as computed by the ABCI code for the second bellow choice.*
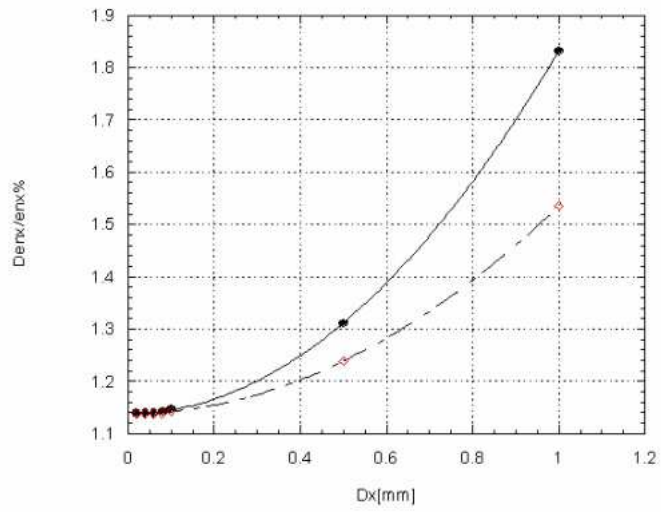
Figure 5.5: *Degradation of the horizontal (full circle) and vertical emittance due to a possible bellow misalignment.*
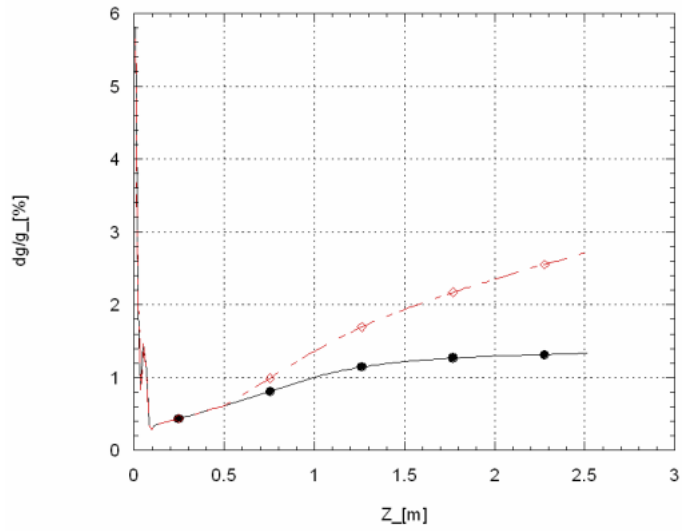

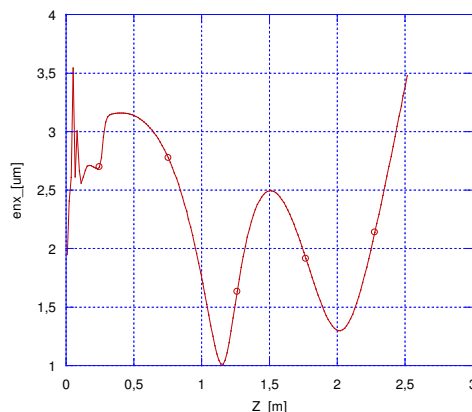Figure 5.6: *Energy spread vs z with (full circle) and without bellow.*

Figure 5.7: *Emittance double minimum behavior.*

It's worth noting the $z = 150cm$ position represents the emittance maximum along the photo-injector and it is the position at which the linac structure should be positioned to get the minimum of the emittance outside the entire linac (see sec. 1.3.2. The emittance value is infact frozen outside the linac structure to the emittance second minimum.

5.2 Misalignment Correction Scheme Study in the SPARC Photo-injector

A bunch can travel off axis for different reasons: for example a laser pointing instability can directly generate the bunch off-axis or the structures can be misaligned. In this case transverse wake fields, RF transverse components and space charge can further push off axis the bunch. Thus the bunch has to be driven to the nominal trajectory with the help of steering magnets, placed along the accelerator structure.

Fig. 5.8 is a conceptual drawing of the steering magnets and the beam position monitors positions along the photo-injector.

A steering is positioned just outside the gun, whilst we place two steering in each traveling wave structure. One more steer is placed at the end of the
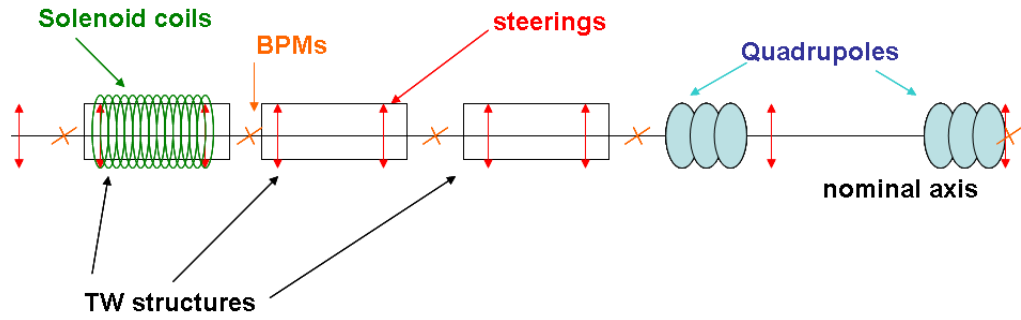
Figure 5.8: *Steering magnets and beam position monitors position in the Sparc photo-injector.*
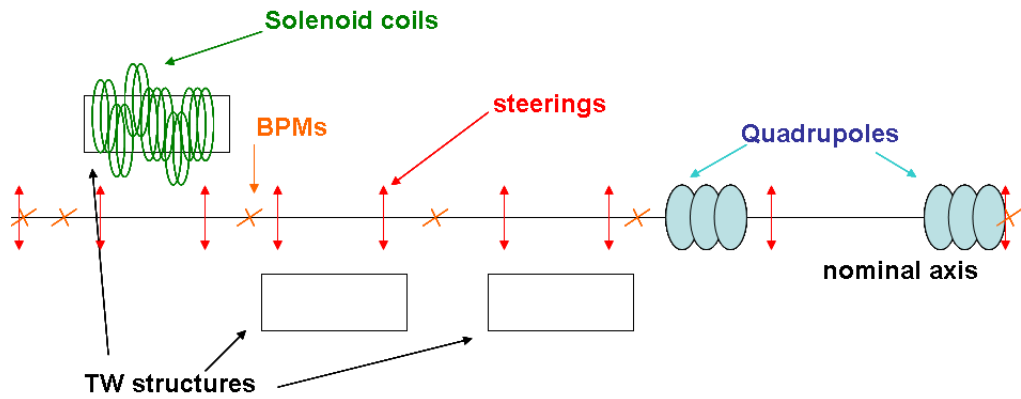
Figure 5.9: *Traveling waves and solenoid coils misalignments in the Sparc photo-injector.*

linac, after the focusing quadrupoles and finally we can find the last steer just before the undulator. Outside the linac beam position monitors are placed after every steering whilst they are placed after every two steerings inside the linac structure.

As a preliminary study of the emittance degradation, we analyze a case for which the bunch's centroid is driven further and further from the nominal axis as shown in fig. 5.9.

The bunch is generated on axis whilst the traveling waves can be transversally displaced with respect the nominal axis; besides the thirteen coils form-

ing the solenoid of the first traveling wave can be independently displaced as well: a study of different misaligned combination for the solenoid coils shows which is the configuration that drives the centroid further from the nominal axis.

Tab. 5.2 shows the solenoid coils and traveling waves misaligned configuration. It's worth noting the mechanical design guarantee $0.05mm$ offset, anyway the standard misalignment chosen in the analysis is $0.1mm$.

Device	$\mathbf{\Delta x mm}$	$\mathbf{\Delta y mm}$
Solenoid coil 1	0.0	0.1
Solenoid coils 2-3-4-5-6	0.1	0.0
Solenoid coils 7-8-9-10-11-12-13	0.0	-0.1
TW1	0.1	0.1
TW2	-0.1	-0.1
TW3	-0.1	-0.1

Table 5.2: Solenoid coils and traveling wave misalignment.

To calculate the right angle in the vertical and horizontal plane that correct the trajectory, we use a transfer matrix between two points, for example the steering and the following BPMs or two adjacent steerings

$$
\begin{pmatrix} x \\ x' \\ y \\ y' \end{pmatrix}_2 = \begin{pmatrix} a & b & e & f \\ c & d & g & h \\ i & l & o & p \\ m & n & q & b \end{pmatrix} \begin{pmatrix} x \\ x' \\ y \\ y' \end{pmatrix}_1
$$

The matrix calculation is made up of two steps: the first step consists in the calculation of the matrix elements.

Let's turn off the steering magnets, $x' = y' = 0$, we obtain the nominal position on the following steering or BPM, x_{2n} and y_{2n}

$$\begin{cases} x_{2n} = ax_1 + ey_1 \\ y_{2n} = iy_1 + ox_1 \end{cases}$$

Turning on the horizontal steer we get the new positions x_{2k} and y_{2k}

$$\begin{cases} x_{2k} = x_{2n} + bx' \\ y_{2k} = y_{2n} + px' \end{cases} \tag{5.1}$$

From eq. 5.1 we can obtain the matrix element b and p. The same reasoning apply to the determination of the matrix element f and l, turning on the vertical steer:

$$\begin{cases} x_{2k} = x_{2n} + fy' \\ y_{2k} = y_{2n} + ly' \end{cases}$$

The second step determines the horizontal and vertical angle of the steering, being known the matrix element and the position wished on the following steer or BPM:

$$\begin{cases} bx' + fy' = x_2 \\ px' + ly' = y_2 \end{cases}$$

It's worth noting such matrix determines the horizontal and vertical angle for one steering. The general case of more than one steering is solved using the superposition principle thus adding the contribution of each steering coming before the ending point.

The above treatment includes the case the horizontal and vertical plane are coupled, as in a solenoid magnetic field.
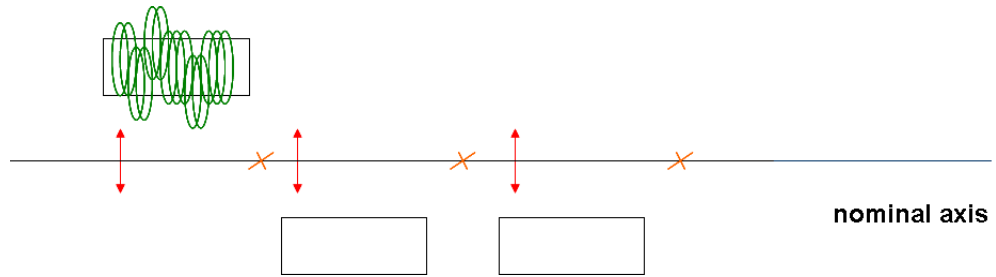
Figure 5.10: *Steering positions and BPMs used in the virtual experiment.*
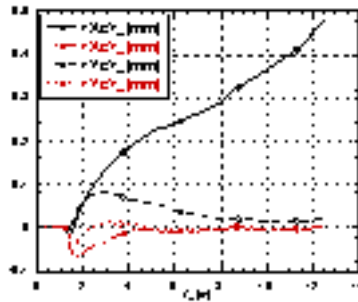
Figure 5.11: *Bunch's centroid position along the structure with and without steering correction.*

5.2.1 Bunch trajectory correction: a virtual experiment

Let's first correct the misaligned configuration trying to drive the centroid trajectory back on the nominal axis. We use the Homdyn code as if we were simulating a virtual experiment; this means we try to align the bunch on the BPMs after each steering and we read the centroid position on the BPMs. Therefore only one steering before each BPMs will be used. The positions of the steerings and BPMs used are sketched in fig. 5.10.

The plots in fig. 5.11 represents the centroid position along the SPARC photo-injector until the linac exit, with and without steering magnets.

Note that the centroid position is successfully driven back to the nominal axis, anyway tab. 5.3 show an emittance which is around $1mmmrad$ but still

Figure 5.12: *Centroid's trajectory drawing along the linac with the bump technique.*

gives rise to an emittance variation of 30%.

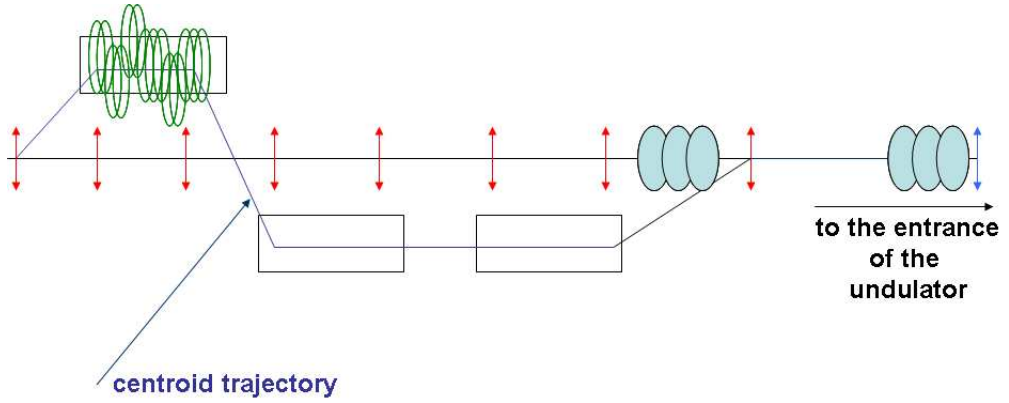| **Offset**	ϵ_{nx} steeroff	ϵ_{nx} steeron	ϵ_{ny} steeroff	ϵ_{ny} steeron
$0.1mm$	$3.47\mu rad$	$1.08\mu rad$	$1.22\mu rad$	$1.06\mu rad$

Table 5.3: Horizontal and transverse emittance with and without steering correction.

The reason is that even if the centroid travels back on the nominal axis, the traveling wave structures are misaligned. Thus the transverse wake fields exists and causes an emittance's increase. Therefore the emittance should be minimized.

5.2.2 Beam Based Alignment: emittance minimization

The beam based alignment technique consists in minimizing a certain parameter, for example the emittance, by forcing the bunch to undergoes bumps and pass along the traveling wave axis as shown in fig. 5.12.

Such technique uses all the steerings placed inside the linac, [19] instead of one per linac as in the previous case. We use again a transfer matrix to
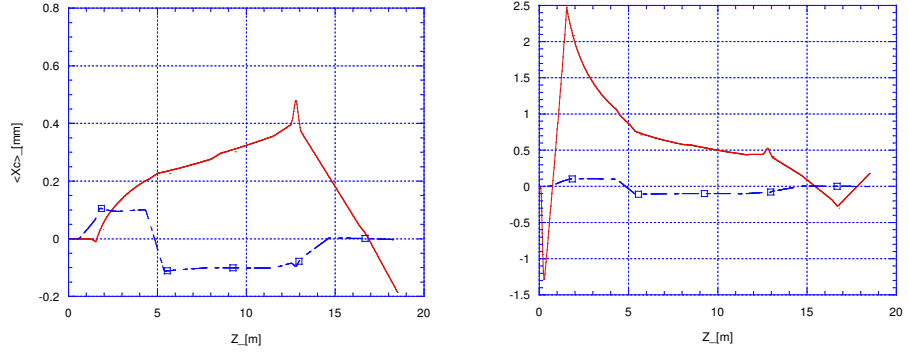
Figure 5.13: *Centroid's trajectory along the linac with the bump technique with and without steering.*

determine the steerings angles; the plots in fig. 5.13 represents the centroid trajectory with and without steerings and demonstrates the centroid travels on the axis of each traveling wave structure as depicted in fig. 5.12.

Tab. 5.4 shows the emittance at the entrance of the undulator after the steering is brought back to the nominal value. Fig. 5.14 shows the emittance evolution until the undulator entrance with and without correction and in the nominal case.

ϵ nominal	ϵ_{nx} steer off	ϵ_{nx} steer on	ϵ_{ny} steer off	ϵ_{ny} steer on
$0.79\mu mm$	$1.81\mu mm$	$0.92\mu mm$	$0.79\mu mm$	$0.92\mu mm$

Table 5.4: Horizontal and transverse emittance with and without steering correction with the beam based alignment technique.

As a conclusion, it's interesting to analyze what happens when, with a given misaligned configuration and fixed steering angles, the bunch is generated off axis; that is a laser pointing instability is present. The plots in fig. 5.15 shows the system is stable and the position and angle at the entrance of the undulator still remains in the range allowed.
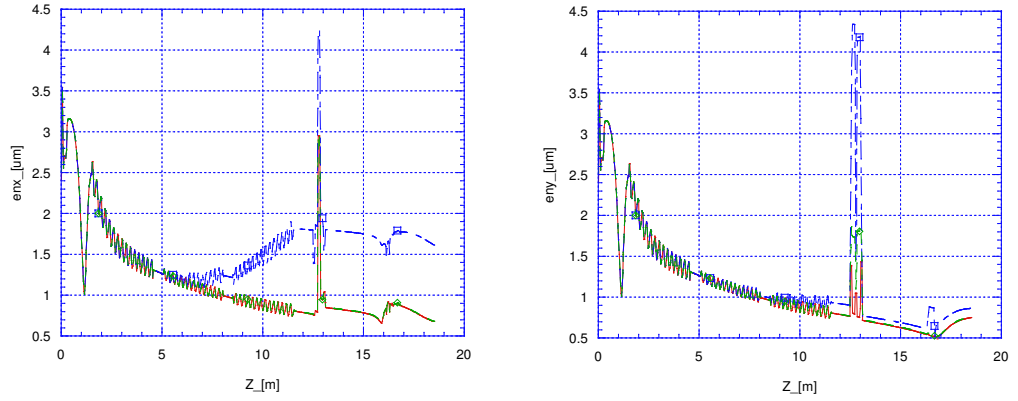
Figure 5.14: *Normalized rms horizontal and vertical emittance, nominal,with and without steering magnets. The correct emittance coincide with the nominal emittance.*
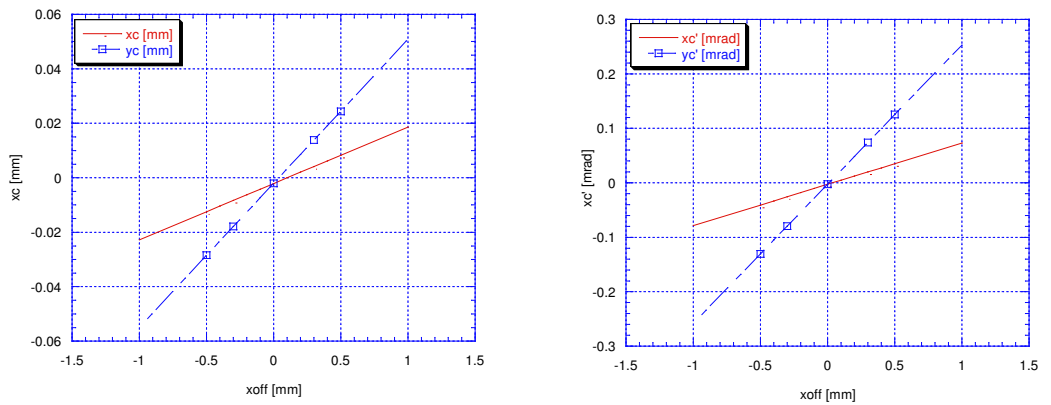
Figure 5.15: *Centroid position and centroid angle at the entrance of the undulator versus the bunch offset at the gun.*

Figure 5.16: *Normalized rms emittance, horizontal end vertical, versus the bunch offset at the gun.*

Finally fig. 5.16 represents the emittance as a function of the laser point instability.

Chapter 6

Conclusions

A high quality beam, that is a low emittance and high current beam, is needed to fulfill FELs' requirements.

The main causes of emittance degradation along the photo-injector, preceding the undulator of the Sparc project, are the so called collective effects.

Collective effects includes space charge and wake fields that have been deeply studied in this work.

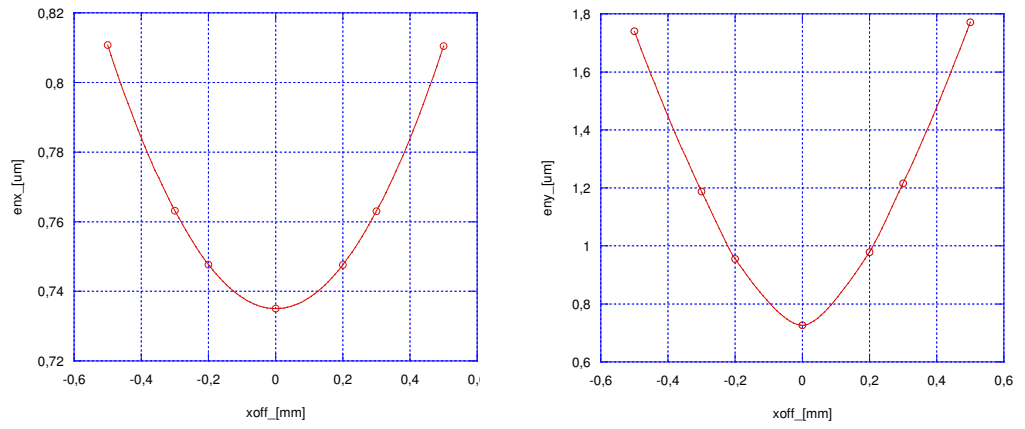Infact by inserting them in a fast semi-analytical code, Homdyn, we could study the emittance degradation and finally compensate the degradation along the photo-injector.The code has been one of the main tool used to study the beam dynamics of the Sparc project.

The space charge is the electromagnetic field produced by a charged bunch. In this work the case of a finite cylindrical bunch with circular cross section, moving at relativistic speed, has been considered. Anyway a more complicate analysis of an elliptical cross section bunch has been studied as well. Infact the focusing properties of some accelerator devices, as quadrupoles and bending magnets, can change the charge distribution of a bunch from round to elliptical.

An approximate analytical solution for the longitudinal electromagnetic field has been obtained, whilst for the transverse electromagnetic field we got numeric solutions. Anyway the study demonstrates a low eccentricity

of the bunch's cross section allows the use of a general rule to obtain the electromagnetic field of an elliptical cross section bunch also for finite length bunch. The general rule give the possibility to associate the transverse electric field on the axis of a round infinite bunch to the electric field of an infinite elliptical one.

The eccentricity involved in the Sparc photo-injector are such that we could apply the general rule in the Homdyn code thus simplifying the computation. Anyway the more complicate equations for the elliptic case should be used in the future second phase of the Sparc project for bunches traveling across magnetic compressors.

The wake fields are the electromagnetic field produced by a charged bunch traveling across devices whose shape is not uniform and/or its resistivity is finite. A wake field can only affect charges following the generating charge. The geometric dimensions of the cavities involved in the Sparc project compared with the bunch's dimension allow the use of the diffraction model to obtain an analytical solution for the longitudinal and transverse wake fields.

Such result was inserted in Homdyn code as well.

Transverse wake fields exists when the bunch travels off axis. Thus we introduced in the code the possibility to study the off axis beam dynamics as well. In this case each slice can be transversally displaced from the nominal axis with respect the neighbor slices; besides it also experiences a transverse deflection due to the space charge forces produced by the neighbor slices.

The improved version of the Homdyn code was successfully compared with the results given by a well known but much slower code as Parmela; thus we used the improved version of the Homdyn code to evaluate the emittance degradation when the bunch travels off axis along the Sparc photo-injector.

In particular a very accurate measure of the emittance evolution downstream the RF gun is required. The movable emittance meter device is used in the Sparc project to measure the emittance along the z axis; it can be moved thank to a bellow structure, whose triangular shape, generates wake

fields. Homdyn allowed the analysis of the emittance degradation and gave the possibility to choose one of the two bellow geometries proposed by the Sparc team.

Moreover, to drive a bunch traveling off axis back to the nominal axis we need an array of steering magnets and beam position monitors. We studied and verified a configuration of steering magnets with the Homdyn code by investigating two types of correction: one correct the bunch's trajectory driving the bunch back to the nominal axis, the other, called beam based alignment technique, looks for the bunch's trajectory giving the minimum for the emittance. We could compensate the emittance with such techniques thus demonstrating the steerings positions chosen are correct.

The whole study was allowed by the Homdyn code, in particular the off-axis version and th wake fields (not included in other code as Parmela) as well as the space charge on centroid has been very useful. Thus beam dynamics is successfully described by the Homdyn code and it was applied to the Sparc project giving an important contribute to the development of the project itself.

Bibliography

[1] H.D. Nuhn. From storage rings to free electron lasers for hard x-rays. Technical Report SLAC-PUB-10300, Stanford Linear Accelerator Center, Menlo Park, CA, December 2003.

[2] E.L.Saldin, E.A.Schneidmiller, and M.V.Yurkov. *The Physics of Free Electron Lasers*, chapter 1-6. Springer, 2000.

[3] The Sparc team. Technical design report for the sparc advanced photo-injector. Technical report, Lab. Nazionali di Frascati-INFN, Frascati, Italy, January 2004.

[4] L.Serafini and J.B. Rosenzweig. Envelope analysis of intense relativistic quasilaminar beams in rf photoinjector: a theory of emittance compensation. *Physical Review E*, 1997.

[5] M.Reiser. *Theory and Design of Charged Particle Beams*, chapter 3. Wiley-Interscience Publication, 1994.

[6] S.Humphries. *Charged Partcle Beams*, chapter 3. Wiley-Interscience Publication, 1990.

[7] J.D.Lawson. *The Physics of Charged Particle Beams*, chapter 3. Clarendon Press-Oxford, 1977.

[8] J. Buon. Beam phase space and emittance. In S. Turner, editor, *Proc. CERN Accelerator School: Fifth General Accelerator Physics Course,*

Finland, 1992, number 94-01 in CERN Yellow Report, pages 89–115, Geneva, Switzerland, 1994. European Lab. for Particle Physics.

[9] C.A.Brau. What brightness means. In *The Physics and Application of High Brightness Electron Beams*, 2002.

[10] L.Serafini. New perspective and programs in italy for advanced applications of high brightness beams. In *The Physics and Application of High Brightness Electron Beams*, 2002.

[11] M.Ferrario, J.E. Clendenin, J.B.Rosenzweig D.T.Palmer, and L.Serafini. Homdyn study for the lcls rf photo-injector. In *The Physics of High Brightness Electron Beams*, 2000.

[12] M.Ferrario, M.Boscolo, V.Fusco, C.Vaccarezza, C.Ronsivalle, J.B.Rosenzweig, and L.Serafini. Recent advanced and novel ideas for high brightness electron beam production based on photoinjectors. In *The Physics and Application of High Brightness Electron Beams*, 2002.

[13] M.Ferrario, V.Fusco, M.Migliorati, L.Palumbo, and B.Spataro. Wake fields effects in the sparc photoinjector. Technical Report SPARC-GE-04/001, Lab. Nazionali di Frascati-INFN, Frascati, Italy, July 2004.

[14] M.Ferrario, V.Fusco, M.Migliorati, L.Palumbo, and B.Spataro. Off-axis beam dynamics in the homdyn code. Technical Report SPARC-BD-04/001, Lab. Nazionali di Frascati-INFN, Frascati, Italy, January 2004.

[15] M.Ferrario, V.Fusco, and M.Migliorati. Electric field for a uniformly charged cylindrical bunch with elliptical cross section. Technical Report SPARC-BD-03/002, Lab. Nazionali di Frascati-INFN, Frascati, Italy, April 2003.

[16] L. Palumbo, V. G. Vaccaro, and M. Zobov. Wake fields and impedance. In S. Turner, editor, *Proc. CERN Accelerator School: Advanced Accel-*

erator Physics Course, Rhodes, 1993, number 95-06 in CERN Yellow Report, pages 331–390, Geneva, Switzerland, 1995. European Lab. for Particle Physics.

[17] K.Bane and M.Sands. Wakefields of very short bunches in an accelerating cavity. In *Proc. Workshop on Impedances Beyond Cut-off, 1987*, 1987.

[18] A.Cianchi and V.Fusco et al. Design study of a movable emittance meter device for the sparc photoinjector. Technical report, Lab. Nazionali di Frascati-INFN, Frascati, Italy, July 2004.

[19] M.Ferrario, V.Fusco, S.Guiducci, M.Migliorati, L.Palumbo, and B.Spataro. Steering correction in the sparc photoinjector. SPARC-BD.

[20] MacMillan. *The Theory of Potential*, chapter 8. Dover Publication, 1930.

[21] O.D.Kellogg. *Foundations of Potential Theory*, chapter 3-7. Springer-Verlag, 1967.

[22] P.Lapostolle. Lectures given in the academic training programme of cern. 1968-1969.

[23] F.J.Sacherer. Rms envelope equation with space charge. *IEEE Trans. nucl. Sci.*, 1971.

[24] M.R.Shubaly. Space charge fields of elliptically simmetrical beams. *Nuclear Instruments and Methods*, 1975.

[25] E.Keil. Diffraction radiation of charged rings moving in a corrugated cylindrical pipe. *Nuclear Instruments and Method*, 1972.

[26] H.Henke. Poin charge pasing a resonator with beam tubes. Technical Report CERN-LEP-RF/85-41, CERN-European Organization for Nuclear Research, November 1985.

[27] J.J.Bisognano. The loss parameter for very short bunches. Technical Report CEBAF-PR-88-005, Southeastern Universities Reasearch Association, 1988.

[28] R.L.Gluckstern. Longitudinal impeance of a periodic structure at high frequency. *Physical Review D*, 1989.

[29] K.Bane. Emittance control for very short bunches. Technical report, Stanford Linear Accelerator Center, Menlo Park, CA, July 2004.

[30] R.B.Palmer. A qualitative study of wake fields for very short bunches. Technical report, Brookhaven national Laboratory, Upton, NY, October 1987.